



1     **Spatial-temporal variations of atmospheric NH<sub>3</sub> concentration and its dry deposition**  
2             **across China based on one decade of satellite and ground-based observations**

3  
4     Fan Sun<sup>1,2</sup>, Yu Cui<sup>1,2</sup>, Jiayin Su<sup>3</sup>, Yifan Zhang<sup>1,2</sup>, Xuejing Shi<sup>1,2</sup>, Junqing Zhang<sup>1,2</sup>, Huili  
5     Liu<sup>1,2</sup>, Qitao Xiao<sup>4</sup>, Xiao Lu<sup>3</sup>, Zhao-Cheng Zeng<sup>5</sup>, Timothy J. Griffis<sup>6</sup>, Cheng Hu<sup>1,2\*</sup>

6     <sup>1</sup> College of Ecology and Environment, Joint Center for sustainable Forestry in Southern China, Nanjing Forestry  
7     University, Nanjing 210037, China

8     <sup>2</sup> Yale-NUIST Center on Atmospheric Environment, Collaborative Innovation Center on Forecast and Evaluation  
9     of Meteorological Disasters (CIC-FEMD), Nanjing University of Information Science & Technology, Nanjing,  
10    210044, China

11   <sup>3</sup> School of Atmospheric Sciences, Sun Yat-sen University, Zhuhai, 519082, China.

12   <sup>4</sup> Key Laboratory of Lake and Watershed Science for Water Security, Nanjing Institute of Geography and  
13   Limnology, Chinese Academy of Sciences

14   <sup>5</sup> School of Earth and Space Sciences, Peking University, Beijing 100871, China

15   <sup>6</sup> Department of Soil, Water, and Climate, University of Minnesota-Twin Cities, Minneapolis, MN, USA

16

17

18

19

20

21

22

23

24   \*Corresponding author: Cheng Hu ([chenghu@njfu.edu.cn](mailto:chenghu@njfu.edu.cn) or [chenghu@umn.edu](mailto:chenghu@umn.edu))

25

26

27

28

29



30 **Abstract:** Ammonia ( $\text{NH}_3$ ), a key alkaline gas in the atmosphere, significantly influences  
31 ecosystem nitrogen cycling and the formation of fine particulate matter ( $\text{PM}_{2.5}$ ). However,  
32 limited ground-based monitoring hinders understanding of  $\text{NH}_3$ 's spatial and temporal  
33 dynamics and its dry deposition across China, which is ranked as one of global largest  $\text{NH}_3$   
34 emission hotspots. This study integrated 2013–2023 satellite-derived  $\text{NH}_3$  column  
35 concentrations from the Cross-track Infrared Sounder (CrIS) with ground in-situ observations.  
36 We used the GEOS-Chem transport model and a random forest algorithm to simulate  $\text{NH}_3$  dry  
37 deposition fluxes and explore the driving forces behind observed trends. Our results show that  
38  $\text{NH}_3$  concentrations were the highest in the North China Plain ( $>10$  ppb), with notable annual  
39 and seasonal increases.  $\text{NH}_3$  concentration in 2023 were 14–31% higher than in 2013. CrIS  
40 retrievals aligned well with in-situ data, though were generally about twice as high. Dry  
41 deposition fluxes exhibited a clear east-west gradient, with maxima in the North China Plain  
42 and Sichuan Basin. Increases in  $\text{NH}_3$  concentrations and deposition were most pronounced in  
43 urban, cropland, and forest regions, with urban areas experiencing the fastest growth and  
44 grasslands the highest total deposition. The national mean  $\text{NH}_3$  concentration and dry  
45 deposition flux were 4.98 ppb and  $0.51 \text{ g m}^{-2} \text{ yr}^{-1}$ , respectively. Anthropogenic emissions  
46 explained 77% of the variability in  $\text{NH}_3$  concentration trend, while meteorological factors  
47 accounted for the remainder. 70%–80% of deposition trend was governed by atmospheric  $\text{NH}_3$   
48 concentration changes. This study highlights growing ammonia pollution and informs nitrogen  
49 management strategies in China.

50



## 51 **1 Introduction**

52 Ammonia (NH<sub>3</sub>), as the most abundant alkaline gas in the atmosphere, readily reacts with acidic  
53 species such as nitric acid and sulfuric acid to form secondary inorganic aerosols. These  
54 aerosols contribute significantly to fine particulate matter (PM<sub>2.5</sub>), thereby adversely affecting  
55 human health, air quality, and atmospheric visibility (Na et al., 2007; Hauglustaine et al., 2014;  
56 He et al., 2001). Reducing NH<sub>3</sub> emissions has been identified as a cost-effective strategy for  
57 mitigating air pollution (Pinder et al., 2007; Wu et al., 2016). Besides, excessive atmospheric  
58 NH<sub>3</sub> can also deposit onto terrestrial and aquatic ecosystems through dry and wet processes,  
59 leading to soil acidification, eutrophication, and biodiversity loss (Hernández et al., 2016; Fu et  
60 al., 2017; Hu et al., 2021). Therefore, monitoring and quantifying atmospheric NH<sub>3</sub>  
61 concentrations and deposition rates within different land use, especially at global emission  
62 hotspots, are critical for informing nitrogen management strategies and protecting air, soil, and  
63 water resources, as well as human health (Liu et al., 2017a; Griffis et al., 2019).

64

65 As the world's largest agricultural country, China is also among the top NH<sub>3</sub> emitters globally,  
66 with an estimated annual emission of 8.4 Tg NH<sub>3</sub> yr<sup>-1</sup>—far exceeding emissions from Europe  
67 (3.1 Tg yr<sup>-1</sup>) and North America (2.8 Tg yr<sup>-1</sup>) (Paulot et al., 2014). In recent years, the  
68 proportion of NH<sub>3</sub> deposition in total nitrogen (N) deposition has been increasing steadily,  
69 accounting for approximately 67% in China by 2020 (Liu L et al., 2024). This upward trend is  
70 expected to continue, driven by declining NO<sub>x</sub> emissions due to pollution control policies and  
71 rising NH<sub>3</sub> emissions associated with global agricultural intensification (Erisman et al., 2008;  
72 Goldberg et al., 2021; Pinder et al., 2008).

73

74 NH<sub>3</sub> deposition in China is nearly double that of the EU (Liu L et al., 2024), mainly due to  
75 excessive nitrogen fertilizer application. In 2014, agricultural NH<sub>3</sub> volatilization accounted for  
76 12 Tg N yr<sup>-1</sup> globally, with China contributing about 34% (Ma et al., 2020). Anthropogenic  
77 activities have nearly doubled NH<sub>3</sub> emission over the past few decades, with cropland and  
78 livestock sources making up around 80% of the global total emissions. Non-agricultural  
79 sources—such as wastewater treatment, human excreta, and transportation—remain relatively  
80 minor (Behera et al., 2013; Zhu et al., 2015; Van Damme et al., 2018). Although the growth rate



81 of both agricultural and non-agricultural emissions has slowed in recent years, the absolute  
82 emissions continue to rise (Chen J et al., 2023).

83

84 Atmospheric  $\text{NH}_3$  concentration serves as a key indicator of emission intensity; therefore,  
85 accurately quantifying its spatiotemporal variations and identifying the underlying drivers is  
86 essential for constraining emission estimates, evaluating the ecological and environmental  
87 impacts and informing effective mitigation strategies. Due to its high reactivity and  
88 predominant agricultural sources,  $\text{NH}_3$  exhibits pronounced temporal and spatial variability. To  
89 date, China operates two national observation networks dedicated to monitoring  $\text{NH}_3$   
90 concentrations and deposition: The National Nitrogen Deposition Monitoring Network  
91 (NNDMN, established in 2004) and the Ammonia Monitoring Network of China (AMoN-China,  
92 established in 2015). While these networks provide high-quality measurements, their sparse  
93 spatial coverage limits their ability to characterize regional patterns, even in the most advanced  
94 global networks (Liu et al., 2017a; b). Additionally, few sites offer long-term (>10 years)  
95 continuous data records (Wang et al., 2023), posing challenges for trend analysis. The limited  
96 availability of  $\text{NH}_3$  monitoring data impedes our understanding of its spatial-temporal patterns  
97 and impacts on air quality, climate, and ecosystems.

98

99 In addition to surface monitoring, the chemical transport models (CTMs, i.e. GEOS-Chem,  
100 WRF-Chem) are widely used to simulate  $\text{NH}_3$  concentrations and dry deposition, as they  
101 incorporate processes such as emission, transport, deposition, and chemical transformation (Hu  
102 et al., 2020; 2021; Lu et al., 2020). However, their accuracy is constrained by uncertainties in  
103 emission inventories and model parameterizations, where the bias in both  $\text{NH}_3$  emissions and  
104 other pollution species (e.g.  $\text{NO}_x$  and  $\text{SO}_2$ ) can lead to considerable uncertainty in simulating  
105  $\text{NH}_3$  concentration and corresponding deposition to ground (Van Der Graaf et al., 2022; Liu et  
106 al., 2024).  $\text{NH}_3$  emission estimates remain highly uncertain due to outdated activity data, poorly  
107 constrained emission factors, and underrepresented sources as cities. Compared to other air  
108 pollutants,  $\text{NH}_3$  exhibits greater variability and uncertainty, particularly because of its diverse  
109 agricultural sources (Beusen et al., 2008; Behera et al., 2013).

110



111 Recent advances in satellite remote sensing offer new opportunities to monitor atmospheric  
112 NH<sub>3</sub>. The first global NH<sub>3</sub> distribution map was derived in 2009 using data from the Infrared  
113 Atmospheric Sounding Interferometer (IASI) onboard the MetOp-A satellite. Since then, other  
114 hyperspectral infrared instruments, such as the Cross-track Infrared Sounder (CrIS), the  
115 Atmospheric Infrared Sounder (AIRS), the Tropospheric Emission Spectrometer (TES) and the  
116 Geostationary Interferometric Infrared Sounder (GIIRS) on board China's FengYun-4B satellite,  
117 have been used to retrieve NH<sub>3</sub> columns (Shephard et al., 2015; Someya et al., 2020; Chen J et  
118 al. 2023; Zeng et al., 2023). Satellite observations provide wide spatial coverage and continuous  
119 temporal resolution, helping to fill gaps in ground networks. Satellite-derived NH<sub>3</sub> data  
120 represent column-averaged values, and the lowest atmospheric level from satellite retrievals  
121 mainly represents averages within the boundary layer height. Therefore, satellite retrievals  
122 cannot directly replace surface-level concentrations which are critical for dry deposition  
123 estimation, which heavily depends on near-surface NH<sub>3</sub> levels and deposition velocities (Lei et  
124 al., 2021; White et al., 2023; Liu S et al., 2024).

125  
126 Despite these limitations, satellite observations have been increasingly used to constrain NH<sub>3</sub>  
127 emissions, assess deposition flux, and identify trends (Chen et al., 2021; Kharol et al., 2018;  
128 Van Damme et al., 2021). For instance, Liu L et al. (2019) estimated global surface NH<sub>3</sub>  
129 concentrations from IASI data and identified high concentrations ( $>6 \mu\text{g N m}^{-3}$ ) in the North  
130 China Plain and northern India. Linear trend analysis from 2008 to 2016 revealed strong  
131 increases in eastern China ( $>0.2 \mu\text{g N m}^{-3} \text{ yr}^{-1}$ ). More recently, satellite data have been used to  
132 investigate urban NH<sub>3</sub> concentrations globally, showing a significant rise ( $1.2\% \text{ yr}^{-1}$ ) in 2008–  
133 2019 (Liu S et al., 2024). These studies demonstrate the utility of satellite retrievals in  
134 characterizing NH<sub>3</sub> pollution and its spatiotemporal evolution, especially in regions lacking  
135 surface monitoring.

136  
137 With the growing importance of NH<sub>3</sub> in nitrogen deposition—now comprising the majority of  
138 dry N deposition (Russell et al., 2003)—accurate estimation of NH<sub>3</sub> dry deposition is becoming  
139 increasingly critical. Kharol et al. (2018) reported that NH<sub>3</sub> contributed more than NO<sub>2</sub> to dry  
140 N fluxes over much of North America in the warm season. Liu L et al. (2019) used satellite-



derived data to estimate global  $\text{NH}_3$  dry deposition during 2008–2016, with results broadly consistent with ground measurements, highlighting the potential for remote sensing to fill spatial gaps in deposition assessment. In China, satellite observations show that high  $\text{NH}_3$  concentrations are mainly concentrated in the North China Plain, Northeast China, and the Sichuan Basin, while low concentrations are found on the Tibetan Plateau (Liu et al., 2017b). However, long-term studies remain scarce, and the drivers of spatiotemporal variation in  $\text{NH}_3$  concentrations and dry deposition under rapid urbanization, land-use change, climate change, and shifts in fertilizer use have not been fully quantified, remaining as a large knowledge gap in understanding and constrain global nitrogen cycle at these emission hotspots.

To robustly constrain and quantify the spatiotemporal variations in near-surface  $\text{NH}_3$  concentrations and dry deposition over the past decade, we integrated multiple data sources and analytical approaches. These included high-resolution satellite-derived  $\text{NH}_3$  retrievals from 2013 to 2023, ground-based observational datasets, simulations from the GEOS-Chem chemical transport model, and dry deposition velocity estimates derived using a random forest algorithm. This study aims to address the following key scientific questions: (1) What are the spatiotemporal patterns of near-surface  $\text{NH}_3$  concentrations across different land cover types in China over the past decade? (2) What are the temporal trends in  $\text{NH}_3$  dry deposition across China during this period, and what are the primary driving factors? (3) How do  $\text{NH}_3$  concentrations and dry deposition in China compare with those in other regions of the world? By addressing these questions, this study seeks to advance understanding of the nitrogen cycle in China and provide a scientific foundation for evaluating ecological impacts and informing targeted strategies for nitrogen management and sustainable agriculture.

## 2 Materials and Methods

### 2.1 Satellite-based atmospheric $\text{NH}_3$ concentration

The satellite-based atmospheric  $\text{NH}_3$  concentration used in this study is CrIS (version 1.6.4). The CrIS is a hyperspectral infrared sounder onboard the Suomi National Polar-orbiting Partnership (Suomi NPP) and NOAA-20 satellites (Shephard et al., 2020). Operating in a sun-synchronous orbit at an altitude of approximately 824 km, CrIS provides global coverage twice



daily, with local overpass time around 13:30 (daytime) and 01:30 (nighttime). The instrument has a swath width of up to 2200 km, with a nadir spatial resolution of approximately 14 km (Zavvalov et al., 2013). CrIS onboard Suomi NPP operated from May 2012 to May 2021, while that onboard NOAA-20 has been operational since March 8, 2019.

In this study, the lowest atmospheric layer of CrIS-derived  $\text{NH}_3$  concentrations was utilized, representing the column average from the surface to approximately 900 m above ground level. As this study focuses on China, we used  $\text{NH}_3$  data over regions of  $73^\circ\text{--}136^\circ\text{E}$  and  $3^\circ\text{--}54^\circ\text{N}$ . To ensure data reliability, only high-quality retrievals were included, filtered using a Quality Flag (QF)  $\geq 3$  and Cloud\_Flag = 0. The analysis period spans from 2013 to 2023, covering both satellite missions, and provides an 11-year, near-continuous time series of atmospheric  $\text{NH}_3$  observations over China. To assess the consistency between the two satellite missions, a regression analysis was performed using monthly averaged  $\text{NH}_3$  concentrations from the overlapping period (2019–2021), revealing strong agreement across China (Figure S1, *SI*). For subsequent analyses, the original satellite retrievals were resampled to a uniform spatial resolution of  $0.1^\circ \times 0.1^\circ$ .

## 2.2 Ground-based observations of atmospheric $\text{NH}_3$ concentration

The dry deposition of  $\text{NH}_3$  is the product of ground level (usually calculated by site-based observations of 1–1.5 m height)  $\text{NH}_3$  concentration and dry deposition velocity. Our previous observation and modeling study in U.S. Corn Belt has found significant vertical gradient within boundary layer height (~1–2 km) (Griffis et al., 2019; Hu et al., 2020; 2021), therefore, the column-averaged  $\text{NH}_3$  concentration should be converted to ground level, which will further used to derive dry deposition flux. To validate and calibrate satellite-derived  $\text{NH}_3$  concentrations, we used measurements from the National Nitrogen Deposition Monitoring Network (NNDMN), which was established since 2010 and comprises 43 monitoring sites across China, encompassing different land use types especially for urban, rural (cropland), and background (coastal, forest, and grassland) regions. The network provides high-quality observations of atmospheric reactive nitrogen (Nr) species in gas, particulate, and precipitation phases, including measurements of both wet and dry nitrogen deposition (Xu et al., 2015).



201 NNDMN employs two monitoring methods: the long-term active denuder for long-term  
202 atmospheric sampling (DELTA) and the low-cost, passive Active Leading Passive High  
203 Absorption (ALPHA) sampler (Flechar et al., 2011). Monthly surface  $\text{NH}_3$  concentrations are  
204 primarily monitored using DELTA, with a few sites utilizing ALPHA. Xu et al. (2015)  
205 demonstrated that these two methods yield statistically consistent  $\text{NH}_3$  measurements.  
206 Considering the typically low  $\text{NH}_3$  concentrations at background sites, this study selected 24  
207 representative urban and rural stations for calibration to improve the reliability of subsequent  
208  $\text{NH}_3$  dry deposition estimates. The locations of monitoring sites and land cover types across  
209 China are shown in Figure. 1a.

210

### 211 **2.3 Estimation of $\text{NH}_3$ dry deposition**

212 Dry deposition flux of atmospheric  $\text{NH}_3$  was estimated by multiplying the surface  $\text{NH}_3$   
213 concentration with the dry deposition velocity, following the equation:

$$214 \quad F = C \times V_d \quad (1)$$

215 Here,  $F$  denotes the dry deposition flux,  $C$  is the surface  $\text{NH}_3$  concentration (ppb) obtained from  
216 satellite retrievals and subsequently corrected using ground-based measurements, and  $V_d$  is the  
217 dry deposition velocity ( $\text{cm s}^{-1}$ ), which is highly variable in space and time due to its sensitivity  
218 to land surface characteristics and meteorological conditions.

219

220 The most widely used approach to derive  $V_d$  is by model simulation, here we first used the  
221 GEOS-Chem chemical transport model to simulate spatial-temporal varied  $V_d$  across China.  
222 However, considering the GEOS-Chem model requires substantial computational resources for  
223 one decade, and to further improve spatial resolution and computational efficiency, a random  
224 forest machine learning algorithm was then applied to simulate dry deposition velocities based  
225 on output from GEOS-Chem model (see more details in Section 2.4).

226

### 227 **2.4 Simulation of Dry Deposition Velocity**

#### 228 **2.4.1 Simulation of $V_d$ by using GEOS-Chem model**

229 We applied a hybrid modeling approach that combines the GEOS-Chem model with a random





230 forest regression algorithm to estimate  $\text{NH}_3$  dry deposition velocities across China. GEOS-  
231 Chem is a global 3-D chemical transport model driven by meteorological inputs from NASA's  
232 Goddard Earth Observing System (GEOS), developed for simulating atmospheric composition  
233 and chemistry (Eastham et al., 2014). In this study, we used GEOS-Chem v13.3.1 to simulate  
234  $\text{NH}_3$  dry deposition velocity over China for the year 2015. The model was driven by assimilated  
235 meteorological data from NASA's MERRA-2 reanalysis. Simulations were conducted on a  
236 nested horizontal grid of  $0.5^\circ \times 0.625^\circ$  covering the domain of  $60^\circ\text{E}$ – $149.375^\circ\text{E}$  and  $11^\circ\text{S}$ –  
237  $54.5^\circ\text{N}$  (Lu et al., 2024).

238

#### 239 **2.4.2 Simulation of $V_d$ by using random forest machine learning algorithm**

240 To improve the spatial resolution and model efficiency, we used the GEOS-Chem model based  
241  $V_d$  simulations to train a random forest model that can predict dry deposition velocities under  
242 various meteorological and land surface conditions and with finer spatial resolution for decade's  
243 period. This data-driven approach enables downscaling to a  $0.25^\circ$  resolution and extends  
244 predictions to whole study period from 2013 to 2023 by using ERA5 reanalysis data.

245

246 The random forest (RF) algorithm is a widely adopted ensemble machine learning method that  
247 integrates multiple decision trees using the bagging strategy to capture complex nonlinear  
248 relationships between predictors and response variables. This approach is widely used in  
249 atmospheric environment assessments, nitrogen management in agriculture, and model  
250 validation studies, providing a robust framework for evaluating the ecological impacts of  $\text{NH}_3$   
251 deposition (Asadi et al., 2021; Ai et al., 2024; Zhang et al., 2024). As shown in Figure. S2, the  
252 RF model was trained on multiple bootstrapped datasets and evaluated by aggregating outputs  
253 from multiple trees to obtain stable and accurate predictions. We selected five meteorological  
254 variables from ERA5 reanalysis data as predictors: planetary boundary layer height, 10 m wind  
255 speed, volumetric soil water of surface layer, surface temperature, and total precipitation. The  
256 dataset was randomly split into a training set (60%) and a validation set (40%), the comparisons  
257 between using two approaches will be evaluated in Section 3.4.1.

258

#### 259 **2.5 Geographical division in China and other supporting data**



260 To investigate spatial heterogeneity in interannual trends, China was divided into nine  
261 subregions based on the classification system from the Resource and Environmental Science  
262 Data Center (Figure. 1b). These regions include: Northeast China Plain, Yunnan–Guizhou  
263 Plateau, Northern Arid and Semi-Arid Region, Southern China, Sichuan Basin and Surrounding  
264 Areas, Middle–Lower Yangtze Plain, Qinghai–Tibet Plateau, Loess Plateau, and Huang–Huai–  
265 Hai Plain. Table 1 summarizes the dominant land cover types and their proportional areas within  
266 each subregion, and the provinces contained in each region are listed in Table S1 (*SI*), the details  
267 of main land use categories and corresponding proportions in each region are also displayed in  
268 Figure 1b and Text S2 (*SI*).

269

270 To clarify the characteristics of atmospheric  $\text{NH}_3$  concentrations and dry deposition flux across  
271 different land surface types, we utilized the 30-meter resolution China annual Land Cover  
272 Dataset (CLCD) to classify surface types. The CLCD is the first annual land cover product for  
273 China derived from Landsat imagery, covering the period from 1985 to 2022 (Yang et al., 2021).  
274 The dataset categorizes land cover into nine classes: cropland, forest, shrubland, grassland,  
275 water bodies, snow/ice, bare land, impervious surfaces, and wetlands. Based on this  
276 classification, we conducted a systematic analysis of the spatial variation and temporal trends  
277 in  $\text{NH}_3$  concentrations and dry deposition fluxes across different land surface types.

278

279 In this study, multiple emission inventories of  $\text{SO}_2$ ,  $\text{NO}_x$ , and  $\text{NH}_3$  were utilized to investigate  
280 the drivers behind changes in atmospheric  $\text{NH}_3$  concentrations and to assess potential future  
281 trends. The emission inventories for  $\text{SO}_2$  and  $\text{NO}_x$  include: (1) the Inversed Emission Inventory  
282 for Chinese Air Quality (CAQIEI, <https://www.scidb.cn/en/detail?dataSetId=81cc0de9c68b4a4981e2f295ac612fbf>); (2) the  
283 Multi-resolution Emission Inventory for China (MEIC, [http://meicmodel.org.cn/?page\\_id=560](http://meicmodel.org.cn/?page_id=560)); (3) the Air Benefit and Cost and Attainment  
284 Assessment System - Emission Inventory (ABaCAS, [https://abacas-](https://abacas-dss.com/abacasChinese/Default.aspx)  
285 [dss.com/abacasChinese/Default.aspx](https://abacas-dss.com/abacasChinese/Default.aspx)); (4) the Community Emissions Data System (CEDS,  
286 <https://github.com/JGCRI/CEDS/>); and (5) the Emissions Database for Global Atmospheric  
287 Research (EDGAR, [https://edgar.jrc.ec.europa.eu/dataset\\_ap81#p3](https://edgar.jrc.ec.europa.eu/dataset_ap81#p3)). Due to the relatively late  
288  
289



development of ammonia ( $\text{NH}_3$ ) research and the limited availability of comprehensive emission inventories, this study employed only two datasets—EDGAR v8.1 and MEIC—for  $\text{NH}_3$  emission analysis. In addition, the Dynamic Projection model for Emissions in China (DPEC, [http://meicmodel.org.cn/?page\\_id=1917](http://meicmodel.org.cn/?page_id=1917)), developed by Tsinghua University, was used to project future emission trends. Further details on all six emission inventories are provided in Text S3 and Table S2 (SI).

## **2.6 Quantification of influencing factors to annual trend of $\text{NH}_3$ concentration and dry deposition**

### **2.6.1 Simulation of ground $\text{NH}_3$ concentration by using random forest model**

To assess the contributions of meteorological conditions and emissions to  $\text{NH}_3$  concentrations over study period, we constructed another random forest model to simulate atmospheric  $\text{NH}_3$  concentration, where the CrIS-retrieved  $\text{NH}_3$  concentrations for 2022 were used as the model output considering the most updated emission inventory is available for 2022, and input parameters included five ERA5-derived meteorological variables (boundary layer height, wind speed, soil moisture, temperature, and precipitation) and three emission datasets from the EDGAR inventory ( $\text{SO}_2$ ,  $\text{NO}_x$ , and  $\text{NH}_3$  emissions). To isolate the effects of emissions and meteorology, we conducted a sensitivity experiment using the 2022-trained model as the baseline. By holding emissions constant or regressing meteorological data back to 2013 (and vice versa), we simulated  $\text{NH}_3$  concentrations attributable solely to changes in meteorology or emissions. The contributions of each factor were then normalized to calculate the percentage influence on  $\text{NH}_3$  concentration changes.

### **2.6.2 Quantification of influencing factors to annual trends of $\text{NH}_3$ concentration**

We further used the logarithmic differentiation method to decompose the relative contributions of  $\text{NH}_3$  concentration and dry deposition velocity to the overall change in dry deposition flux. The logarithmic form allows the multiplicative relationship to be transformed into an additive form, making it suitable for quantifying variable impacts, particularly when concentration and velocity change in opposite directions. The decomposition is based on the following:



319 
$$\Delta \ln F = \Delta \ln C + \Delta \ln V_d \quad (2)$$

320 The respective contributions of concentration and deposition velocity are calculated as:

321 
$$\eta_C = \left| \frac{\Delta \ln C}{\Delta \ln F} \right| \quad (3)$$

322 
$$\eta_{V_d} = \left| \frac{\Delta \ln V_d}{\Delta \ln F} \right| \quad (4)$$

323 where  $\Delta \ln$  denotes the change in the natural logarithm,  $\eta_C$  and  $\eta_{V_d}$  represent contributions  
324 from  $\text{NH}_3$  concentration and dry deposition velocity. These contributions were normalized to  
325 provide intuitive percentage values. This method is particularly effective in quantifying  
326 dynamic and opposing changes and does not assume linear relationship, offering a more robust  
327 analysis than traditional linear regression. Additionally, the Mann-Kendall (MK) trend test was  
328 employed to statistically evaluate the temporal trends in  $\text{NH}_3$  concentrations over the study  
329 period.

330

### 331 **3 Results and Discussions**

#### 332 **3.1 Spatial patterns of near-surface $\text{NH}_3$ concentration and its trend analysis**

333 Using CrIS satellite-derived near-surface  $\text{NH}_3$  concentrations from 2013 to 2023, we generated  
334 a high-resolution ( $0.1^\circ \times 0.1^\circ$ ) monthly averaged dataset of  $\text{NH}_3$  distributions across China over  
335 an 11-year period. We first displayed the annual averaged spatial patterns and its trend from  
336 2013-2023 at both the national scale and within specific subregions, followed by an analysis of  
337 seasonal variations (Figures. 2a–j and Figures. S3–S7, *SI*). The results of annual average from  
338 indicate that the North China Plain (also known as the Huang-Huai-Hai Plain) consistently  
339 exhibited the highest  $\text{NH}_3$  concentrations ( $>10$  ppb) during the study period (Figure 2a). This  
340 region is recognized as one of China's most intensive agricultural zones, accounting for  
341 approximately 25% of China's total arable land area and grain production (Song et al., 2024),  
342 and is thus subject to frequent fertilizer application, contributing significantly to elevated  $\text{NH}_3$   
343 emissions.

344

345 The secondary  $\text{NH}_3$  concentration hotspots were observed in the Guanzhong Plain in Shaanxi



Province and the southeastern margin of the Tibetan Plateau. The Guanzhong Plain region is another major agricultural production area in western China, with cultivated land accounting for 49% of Shaanxi Province's total arable area. Intensive fertilizer uses and related activities are the main sources of  $\text{NH}_3$  emissions in this region. The elevated  $\text{NH}_3$  concentrations in southeastern Tibet are likely attributed to emissions from extensive livestock farming, particularly yak and sheep husbandry. In addition to these agricultural and pastoral regions, relatively high  $\text{NH}_3$  concentrations were also observed in arid zones such as Xinjiang and Inner Mongolia. However, these apparent  $\text{NH}_3$  enhancements are likely artifacts of satellite retrievals influenced by surface radiative properties. High surface thermal contrast in desert regions may amplify the apparent  $\text{NH}_3$  spectral signature during the satellite overpass time of midday (13:00), leading to overestimation of  $\text{NH}_3$  concentrations due to limitations in retrieval algorithms and thermal contrast biases (Liu et al., 2020b).

To further explore spatial patterns in temporal change, the pixel-wise trend analysis of annual  $\text{NH}_3$  concentrations was also conducted (Figure. 2b). Significant positive trends ( $>0.4 \text{ ppb yr}^{-1}$ ) were concentrated in the central and eastern parts of China, particularly in major agricultural zones with intensive crop fertilization, where the white areas in the figure indicate trends that were not statistically significant at the 0.05 level. These results are consistent with findings by Warner et al. (2017), who reported a substantial increase in  $\text{NH}_3$  concentrations over eastern China using AIRS data from 2002 to 2016. Our study extends this trend through 2023, indicating that  $\text{NH}_3$  concentrations in these regions have continued to rise significantly in recent years. In contrast, western China generally showed stable or declining trends. Although northern Xinjiang exhibited moderate  $\text{NH}_3$  increases in areas where the trend passed significance testing, other parts of the west demonstrated declining trends. This pattern may be associated with grassland restructuring policies implemented by the Chinese government to reduce overgrazing and restore degraded ecosystems, thereby lowering  $\text{NH}_3$  emissions from pastoral sources.

The spatial patterns of  $\text{NH}_3$  concentration increases correspond closely to regions of high population density and agricultural land use, such as the North China Plain and Sichuan Basin.



376 These areas are also hotspots for reductions in SO<sub>2</sub> and NO<sub>x</sub> emissions due to stringent air  
377 pollution control measures as displayed in Figures. S8–S9 (*SI*). The decline in acid gases may  
378 reduce atmospheric neutralization capacity, thereby enhancing the lifetime and apparent  
379 abundance of NH<sub>3</sub> in the atmosphere (Dong et al., 2023), contributing to the pronounced  
380 upward trends observed in these regions.

381

382 We also displayed the seasonal variations and its trend during 2013–2023, clear seasonal  
383 differences in NH<sub>3</sub> spatial distribution were observed during whole study period (Figure 2c–j,  
384 Figures S4–S7). In spring, the NH<sub>3</sub> distribution resembled the annual pattern but exhibited  
385 concentrations approximately 14% higher. The Huang-Huai-Hai Plain showed especially  
386 concentrated and elevated values, likely due to extensive fertilizer use during spring planting.  
387 In contrast, the northwest exhibited little seasonal deviation from annual averages, as emissions  
388 are more influenced by pastoral activities than by seasonal patterns of fertilization in  
389 agricultural regions. In autumn, NH<sub>3</sub> levels declined sharply, despite localized fertilizer  
390 application, primarily due to reduced emissions and cooler temperatures. High concentrations  
391 remained in Shandong Province and adjacent regions. Winter concentrations were the lowest,  
392 reflecting widespread agricultural dormancy and low temperatures, although lower thermal  
393 contrast and reduced NH<sub>3</sub> signal strength increase retrieval uncertainties.

394

395 In summer, NH<sub>3</sub> concentrations peaked across China, with higher concentration regions  
396 expanding westward into semi-arid areas. This peak seasonality contrasts with trends in Europe  
397 and the U.S., where springtime peak is also more typical. In China, summer fertilization for  
398 maize cultivation—often involving both mineral and organic fertilizers—contributes to the  
399 observed summer peak (Paulot et al., 2014). Elevated temperatures further enhance  
400 volatilization from manure and urban waste, intensifying atmospheric NH<sub>3</sub> levels. Liu et al.  
401 (2024) reported that temperature increases accounted for up to 20% of urban NH<sub>3</sub> increases  
402 between 2008 and 2019. Notably, elevated NH<sub>3</sub> levels were also observed along the Yangtze  
403 River basin, corresponding to fertilizer use in rice paddies.

404

405 The spatial distributions of 11-years' trend analyses for each season are also displayed (Figures



2d, f, h and j), they show significant increases across eastern China, particularly during summer and autumn. Overall, these results indicate the annual trend of surface  $\text{NH}_3$  concentration occurred throughout each season but with obvious seasonal difference. Winter trends were the weakest in magnitude and spatial extent. Consistent with annual patterns, the North China Plain and Sichuan Basin showed the most pronounced increases. Western China showed few significant trends, with slight increases in northern Xinjiang during summer and autumn, and declines in other areas.

413

### 3.2 Temporal variation of near-surface $\text{NH}_3$ concentrations for different regions

We also calculated the temporal variation of annual  $\text{NH}_3$  concentrations and across different seasons from 2013 to 2023 (Figure 3a). Over this period, the annual mean  $\text{NH}_3$  concentration in China increased by 22%, with seasonal increases of 14% in spring, 31% in summer, 26% in autumn, and 18% in winter, respectively. Among these seasons, summer exhibited the highest mean concentration (3.60 ppb), followed by spring (3.28 ppb), with annual, autumn, and winter means recorded at 2.88 ppb, 2.63 ppb, and 2.00 ppb, respectively (Table 2). The Mann-Kendall trend test results (Table 2) indicated statistically significant upward trends for spring, summer, autumn, and annual mean concentrations ( $p < 0.05$ ). Although winter showed a positive trend ( $Z > 0$ ), it did not reach statistical significance. The seasonal rates of increase, in descending order, were: summer (0.065 ppb  $\text{yr}^{-1}$ ), autumn (0.050 ppb  $\text{yr}^{-1}$ ), annual (0.045 ppb  $\text{yr}^{-1}$ ), spring (0.039 ppb  $\text{yr}^{-1}$ ), and winter (0.023 ppb  $\text{yr}^{-1}$ ). The most pronounced increase during summer from 2013 to 2023 also aligns with previous findings by Liu et al. (2018), which only analyze the North China Plain region from 2008 to 2016, but their trend is slightly lower than our results.

428

The summer increasing trend of atmospheric  $\text{NH}_3$  is likely closely related to global warming (Figure S10, SI), previous studies shown that over 40% of fertilizer application and approximately 25% of livestock emissions occur during the summer months (Xu et al., 2015; Kang et al., 2016), which enhances  $\text{NH}_3$  volatilization from ground to atmosphere. The slower rate of increase in spring may be associated with China's national fertilizer reduction policies, such as the "Action Plan for Fertilizer Reduction by 2025". Fertilizer use increased until peaking in 2015 and subsequently declined for eight consecutive years, resulting in a 15.1%



436 reduction from 2013 to 2023, with the national application totaling 50.22 million tons in 2023  
437 (Figure. S11).

438

439 The decrease in chemical fertilizer use, combined with the adoption of organic fertilizers, has  
440 contributed to a gradual slowdown in the rise of  $\text{NH}_3$  concentrations. By 2024, the nitrogen uses  
441 efficiency (NUE) for rice, maize, and wheat reached 42.6%, helping to reduce fertilizer input  
442 without compromising yields and mitigating  $\text{NH}_3$  emissions and nutrient pollution. Zhan et al.  
443 (2020) identified improving NUE as the most effective and cost-efficient strategy for  $\text{NH}_3$   
444 mitigation in agriculture, a finding supported by cost-benefit assessments (Zhang et al., 2020).  
445 Autumn also showed a substantial increase in  $\text{NH}_3$  concentrations, second only to summer.  
446 Current emission reduction efforts have primarily focused on spring and summer, reflecting  
447 crop planting cycles, while autumn has often been overlooked, contributing to this seasonal gap  
448 in mitigation. These findings highlight the need for seasonally and crop-specific emission  
449 control strategies in future  $\text{NH}_3$  management efforts.

450

451 Significant spatial heterogeneity was observed in the interannual variation of  $\text{NH}_3$   
452 concentrations across different regions. Figure 3b illustrates long-term trends in  $\text{NH}_3$   
453 concentrations for nine subregions. Most regions exhibited increasing trends, with the Huang-  
454 Huai-Hai Plain standing out for its consistently elevated concentrations—approximately twice  
455 as high as the national average (Table 3). This region is China's primary agricultural zone,  
456 characterized by high population density and intensive agricultural activity, both of which  
457 contribute to substantial  $\text{NH}_3$  emissions. Additionally, it has been a focal area for  $\text{SO}_2$  and  $\text{NO}_x$   
458 emission reductions, and the combined effects of high emissions and reduced atmospheric  
459 neutralization capacity have led to persistent  $\text{NH}_3$  accumulation.

460

461 MK trend analysis further revealed statistically significant upward trends in the Huang-Huai-  
462 Hai Plain, the Northern Arid and Semi-Arid Region, the Loess Plateau, the Middle-Lower  
463 Yangtze Plain, South China, the Northeast China Plain, and the Sichuan Basin and its  
464 surrounding regions. The Huang-Huai-Hai Plain showed the steepest increase, with an average  
465 annual rise of 0.24 ppb, corresponding to a 7% per year growth rate—3.3 times the national





average. The primary driver of this sharp increase is the marked reduction in atmospheric SO<sub>2</sub>, which has disrupted the NH<sub>3</sub>–acid gas neutralization balance (Xu et al., 2019a). The Loess Plateau ranked second, with an average increase of 0.14 ppb per year. In contrast, the Yunnan–Guizhou Plateau exhibited a mild, non-significant increase, with relatively stable concentrations. The Tibetan Plateau showed a slight downward trend, which also lacked statistical significance ( $p > 0.05$ ), indicating a relatively stable NH<sub>3</sub> regime in this high-altitude, low-emission region.

### **3.3 Comparison between satellite and ground-based NH<sub>3</sub> observations and satellite data correction**

As stated in Section 2.1, although satellite-based observations provide high spatial resolution and long-term data for atmospheric NH<sub>3</sub> studies, they represent near-surface column average between ground to around 1 km, where large vertical gradient has been reported because of its reactive nature of ammonia and its role in chemical transformation processes (Hu et al., 2020; 2021; Griffis et al., 2019). Besides, the dry deposition of NH<sub>3</sub> is the product of ground level (usually calculated by site-based observations of 1–1.5 m height) NH<sub>3</sub> concentration and dry deposition velocity. Therefore, to enable accurate estimation of NH<sub>3</sub> dry deposition, we conducted a comparative analysis between satellite-derived and multiple years observations at 24 ground-based NH<sub>3</sub> sites, and their relationship will be used to correct column averages to ground level height.

As shown in Figure 4a, satellite and ground-based NH<sub>3</sub> concentrations exhibit a strong correlation ( $R = 0.79$ ), with a coefficient of determination ( $R^2$ ) of 0.62 and a root mean square error (RMSE) of 3.56 ppb. However, the ground-based measurements are, on average, approximately twice as high as those retrieved by satellite. This discrepancy can be attributed to the vertical gradient of NH<sub>3</sub> in the atmosphere: ground-based sensors typically operate at heights of 1–1.5 m, while satellite instruments, even in their lowest vertical layer, observe at altitudes hundreds of meters above ground. Many pioneer studies have demonstrated that when the land surface acts as an NH<sub>3</sub> source, its vertical distribution decreases logarithmically with height. For example, our previous studies of tall tower observations in the United States



reported an  $\text{NH}_3$  mixing ratio gradient of  $-0.27$  ppb per 100 m, with modeled gradients ranging from  $-0.21$  to  $-0.84$  ppb per 100 m (Hu et al., 2020; 2021; Griffis et al., 2019), showing good agreement between observations and simulations. When using the gradient of above reported values, the average of 0–1000 m column  $\text{NH}_3$  concentration should be around 1–4 ppb lower than ground level, this pronounced vertical gradient is a major reason for the systematic underestimation of  $\text{NH}_3$  by satellites.

To address this bias, we used the regression relationship derived from Figure 4a to calibrate the satellite retrievals. After correction, a new regression (Figure 4b) shows a nearly 1:1 agreement between satellite and ground-based measurements, with the RMSE reduced to 1.69 ppb. To further assess the correction effectiveness, we selected the year 2015—when both satellite and ground data are available—for analysis. As shown in Figure 4c, the corrected satellite-derived  $\text{NH}_3$  concentrations closely match ground observations across almost all sites, confirming the reliability of the correction approach. This calibration function was then applied to the full 2013–2023 satellite dataset to improve the reliability of  $\text{NH}_3$  dry deposition estimates. Table 3 illustrated the corrected average  $\text{NH}_3$  concentrations across different regions, with the Huang-Huai-Hai Plain exhibiting the highest value of 11.36 ppb. This was followed by the Northern Arid and Semi-Arid Region (6.93 ppb), the Qinghai–Tibet Plateau (6.48 ppb), and the Loess Plateau (6.05 ppb). Although the bias-corrected  $\text{NH}_3$  concentrations in these regions ranked immediately after the Huang–Huai–Hai Plain, their values were approximately two times lower than those observed in the Huang–Huai–Hai Plain.

### 3.4 Estimation of spatial-temporal variations of $\text{NH}_3$ dry deposition across China

#### 3.4.1 Simulation of spatial-temporal dry deposition velocities

To estimate  $\text{NH}_3$  dry deposition flux across China, we first used the GEOS-Chem model to simulate  $\text{NH}_3$  dry deposition velocities for the year 2015 (Figure 5a). Considering the high computational cost and limited temporal flexibility of the GEOS-Chem model, we adopted a hybrid modeling approach by training a random forest (RF) machine learning model on the GEOS-Chem model-based simulation results. This approach allowed us to extend the simulation to the full 2013–2023 period, while improving both spatial resolution and



computational efficiency. The GEOS-Chem-derived 2015 dry deposition velocity served as the response variable for training the RF model.

The resulting RF-predicted dry deposition velocities for 2015 show high spatial agreement with the GEOS-Chem outputs (Figure 5b). Both models identify southern China as a hotspot for dry deposition velocity, likely due to the region's warm and humid conditions that facilitate gaseous  $\text{NH}_3$  deposited onto ground surface. Additionally, southern China is a major rice-producing region where surface resistance in paddy fields is lower than in dryland fields, further enhancing dry deposition rates. Figure 5c shows the differences between the two model outputs, with over 99% of grid cells having discrepancies less than  $0.1 \text{ cm s}^{-1}$ , indicating strong consistency and validating the reliability of the RF model for long-term simulations. Using this trained model, we further simulated  $\text{NH}_3$  dry deposition velocities from 2013 to 2023 at monthly averages.

### 3.4.2 The spatial-temporal variations of $\text{NH}_3$ dry deposition in China

With the corrected spatial-temporal  $\text{NH}_3$  concentrations and simulated deposition velocities from 2013 to 2023, we derived the monthly grid-level  $\text{NH}_3$  dry deposition flux for China. These were further aggregated to estimate flux and total deposition over different surface types (Figure 6, Figure S12, *SI*). Figure 6a illustrates the spatial distribution of  $\text{NH}_3$  dry deposition flux average from 2013 to 2023. Distinct spatial differences are evident, where the eastern coastal regions exhibited significantly higher deposition flux than inland areas, with values higher than  $1.8 \text{ g NH}_3 \text{ m}^{-2} \text{ yr}^{-1}$ . Notably, the Huang-Huai-Hai Plain and the southwestern region of the Qinghai-Tibet Plateau emerged as prominent hotspots of  $\text{NH}_3$  dry deposition, highlighting the substantial impact of intensive agricultural activities and industrial emissions. Elevated deposition rates were also observed in the southern Tibetan Plateau, driven by locally high  $\text{NH}_3$  concentrations.

A trend analysis of dry deposition over the 11-year period (Figure 6b) shows statistically significant increases in deposition flux in eastern coastal areas ( $> 0.1 \text{ g m}^{-2} \text{ yr}^{-1}$ ), likely reflecting rising  $\text{NH}_3$  concentrations in these regions. In contrast, western China shows minimal change, with some areas even exhibiting slight declines. Unlike the  $\text{NH}_3$  concentration trends,



there is no region in western China displayed a statistically significant increase in dry deposition flux, emphasizing the spatial decoupling between emission intensity and deposition patterns in less industrialized regions.

The interannual variation of  $\text{NH}_3$  dry deposition also exhibited significant spatial heterogeneity at the regional scale (Figure 6c and Table 4). The Huang-Huai-Hai Plain, characterized by persistently high  $\text{NH}_3$  concentrations, recorded the highest area-specific dry deposition flux, reaching  $1.06 \text{ g m}^{-2} \text{ yr}^{-1}$ —approximately twice the levels observed in other regions. MK trend analysis indicated a significant increasing trend in dry deposition flux across all regions except the Tibetan Plateau, where a weak downward trend was observed but was not statistically significant. The most pronounced increase was found in the Huang-Huai-Hai Plain, with an average annual increment of  $0.05 \text{ g m}^{-2} \text{ yr}^{-1}$ , followed by the middle and lower reaches of the Yangtze River, at  $0.03 \text{ g m}^{-2} \text{ yr}^{-1}$  (Table 4).

### 3.4.3 Comparisons of $\text{NH}_3$ concentration, dry deposition velocity and flux in different surface categories

In addition to meteorological factors, land cover types play a pivotal role in regulating dry deposition processes. In this section, we annually extracted  $\text{NH}_3$  concentrations, dry deposition velocities, and dry deposition fluxes across different land cover categories. The analysis focused on four representative land-use types—urban, cropland, forest, and grassland—selected based on their distinct  $\text{NH}_3$  emission characteristics (Figure 7; Table S3, *SI*). The average  $\text{NH}_3$  concentrations, ranked from highest to lowest, were: urban (8.76 ppb), cropland (6.27 ppb), national average (6.01 ppb), grassland (5.72 ppb), and forest (3.76 ppb) (Figure 7a). Urban areas exhibited both the highest concentrations and the largest interannual variability, with a statistically significant upward trend ( $p < 0.05$ ,  $Z > 1.96$ ), increasing at an average rate of  $0.39 \text{ ppb yr}^{-1}$ . This trend is primarily attributed to anthropogenic sources such as vehicular emissions, as well as the urban heat island effect, which raises urban temperatures by  $1\text{--}3^\circ\text{C}$ —and occasionally by over  $10^\circ\text{C}$ —relative to surrounding rural areas. These elevated temperatures, further amplified by global warming, facilitate enhanced  $\text{NH}_3$  volatilization.



586 While  $\text{NH}_3$  concentrations over grassland areas remained relatively stable throughout the study  
587 period, cropland regions exhibited a continuous upward trend, with the two trends intersecting  
588 in 2016 (Figure 7a), after which  $\text{NH}_3$  concentrations in croplands exceeded those in grasslands.  
589  $\text{NH}_3$  emissions in grassland ecosystems are predominantly associated with livestock grazing,  
590 and the stabilization observed is likely attributable to the implementation of grazing restrictions  
591 and ecological restoration policies. In contrast, despite the introduction of fertilizer reduction  
592 policies in some agricultural areas, rising food demand driven by population growth has  
593 sustained or even increased fertilizer application, thereby contributing to the observed increase  
594 in cropland  $\text{NH}_3$  levels. At the national scale,  $\text{NH}_3$  concentrations exhibited a statistically  
595 significant upward trend, with an average increase of  $0.1 \text{ ppb yr}^{-1}$  (equivalent to an annual  
596 growth rate of 2.2%). Forested regions, which are minimally impacted by anthropogenic  
597 sources such as synthetic fertilizers and livestock emissions, maintained the lowest and most  
598 stable  $\text{NH}_3$  concentrations, showing only a slight upward trend that may be linked to climate  
599 warming (Figure 7a; Figure 8).

600

601 Dry deposition velocities exhibited limited interannual variability across different land cover  
602 types. Forested areas recorded the highest average deposition velocity, likely attributable to  
603 greater surface roughness and enhanced canopy-induced turbulence, followed by urban and  
604 cropland regions (Figure 7b; Figure 8). The mean  $\text{NH}_3$  dry deposition velocities for forest, urban,  
605 cropland, grassland, and the national average were 0.43, 0.42, 0.40, 0.32, and  $0.36 \text{ cm s}^{-1}$ ,  
606 respectively. Mann–Kendall trend analysis revealed statistically significant increasing trends in  
607 urban and cropland areas, with annual rates of  $0.0013$  and  $0.0012 \text{ cm s}^{-1} \text{ yr}^{-1}$ , respectively.  
608 Although forests maintained the highest mean velocity and exhibited a positive trend, the  
609 change was not statistically significant. At the national scale, deposition velocity showed a weak  
610 but consistent upward trend. In contrast, grassland areas experienced a slight decline in  
611 deposition velocity over the 11-year period, though this trend was not statistically significant.

612

613 Area-specific  $\text{NH}_3$  dry deposition fluxes closely followed the spatial distribution of atmospheric  
614 concentrations across different land cover types (Figure 7c; Figure 8). Urban regions exhibited  
615 the highest mean flux ( $0.88 \text{ g m}^{-2} \text{ yr}^{-1}$ ), followed by cropland areas ( $0.61 \text{ g m}^{-2} \text{ yr}^{-1}$ ). Both



616 urban and national average fluxes demonstrated statistically significant upward trends over the  
617 study period. The steepest increase was observed in urban areas, with a rate of  $0.04 \text{ g m}^{-2} \text{ yr}^{-1}$ —  
618 approximately four times the national average—followed by croplands at  $0.03 \text{ g m}^{-2} \text{ yr}^{-1}$ .  
619 Recent findings (Chen P et al., 2023) suggest that, although fertilizer application has been  
620 partially reduced under agricultural emission control policies, non-agricultural sources—such  
621 as industrial processes and transportation—have become the predominant contributors to  $\text{NH}_3$   
622 emissions in China, particularly concentrated in urban areas. This shift has contributed to  
623 elevated  $\text{NH}_3$  concentrations and enhanced dry deposition fluxes in cities.

624

625 In contrast, forests and grasslands showed relatively stable fluxes, likely due to lower levels of  
626 anthropogenic disturbance. Nevertheless, a statistically significant increasing trend in forest  
627 deposition flux was detected, which may have important ecological implications. Sustained  
628 increases in  $\text{NH}_3$  deposition could lead to adverse effects such as plant nutrient imbalances,  
629 biodiversity loss, and eutrophication of adjacent aquatic systems, potentially compromising  
630 forest health and long-term ecosystem stability. Furthermore, interannual variability in dry  
631 deposition was more pronounced in urban areas, reflecting the dynamic nature of urban  
632 development and emission variability, whereas cropland fluxes exhibited a more gradual trend  
633 in response to evolving fertilizer management practices.

634

635 Trends in total  $\text{NH}_3$  dry deposition across different land cover types generally mirrored those  
636 of area-specific fluxes; however, absolute deposition values were modulated by the extent of  
637 each land category. Grasslands accounted for the largest share of total  $\text{NH}_3$  dry deposition (1.23  
638 Tg), followed by croplands (1.15 Tg), forests (0.92 Tg), urban areas (0.21 Tg), and a national  
639 total of 4.85 Tg. Over the 11-year study period, statistically significant upward trends in total  
640 dry deposition were observed at the national scale, as well as in cropland, forest, and urban  
641 areas, with annual increases of 0.10, 0.05, 0.03, and 0.01  $\text{Tg yr}^{-1}$ , respectively. Although  
642 grasslands also exhibited an increasing trend, it was not statistically significant. Changes in  
643 total  $\text{NH}_3$  deposition are driven not only by atmospheric concentrations and deposition  
644 velocities but also by land-use dynamics (Figure 7d; Figure 8). In particular, the continuous  
645 expansion of urban areas from 2013 to 2023 contributed substantially to the increasing trend in



total urban  $\text{NH}_3$  deposition. These findings highlight the importance of considering both biogeochemical processes and anthropogenic land-use changes in assessing long-term trends in reactive nitrogen deposition.

### **3.5 Simulation of $\text{NH}_3$ concentration and contribution factors analysis to decade's trend for both $\text{NH}_3$ concentration and deposition flux**

In this section, we further investigated the key drivers of atmospheric  $\text{NH}_3$  concentrations using a Random Forest (RF) regression model. Model performance was evaluated by comparing simulated  $\text{NH}_3$  concentrations with observations for the period 2013–2023, showing good agreement (Figure 9). The RF model effectively captured the spatial variability of  $\text{NH}_3$  concentrations, with deviations generally within  $\pm 0.1$  ppb, indicating robust predictive capability. The input variables were categorized into two major groups: meteorological factors and anthropogenic emissions, including direct  $\text{NH}_3$  emissions as well as co-emitted  $\text{SO}_2$  and  $\text{NO}_x$  species.

The RF model simulation results indicated that anthropogenic emissions were the dominant driver, accounting for approximately 77% of the variance in  $\text{NH}_3$  concentrations, while meteorological conditions explained the remaining 23% (Figure 10). Among meteorological parameters, air temperature emerged as the most influential factor, whereas other variables (e.g., relative humidity, wind speed) exhibited minimal interannual variation and lower predictive importance. Analysis of ERA5 reanalysis data revealed a persistent warming trend over the past decade, with the annual mean surface temperature in 2023 being 8.4% higher than in 2013 (Figure S10, *S1*). Previous studies, such as Hu et al. (2020), reported an exponential relationship between  $\text{NH}_3$  mixing ratios and temperature, with  $\text{NH}_3$  concentrations increasing from 4 ppb to 19 ppb as temperature rises from  $0^\circ\text{C}$  to  $10^\circ\text{C}$ . The regional temperature sensitivity ( $Q_{10}$ ) of  $\text{NH}_3$  emissions was estimated to be approximately 2.5, indicating that continued warming will likely enhance  $\text{NH}_3$  volatilization. This may further exacerbate nitrogen loss from agricultural systems and elevate  $\text{NH}_3$  dry deposition to downwind ecosystems, potentially intensifying ecological risks such as eutrophication and biodiversity loss.



676 Figure S13 illustrates multi-year emission trends of SO<sub>2</sub>, NO<sub>x</sub>, and NH<sub>3</sub> derived from multiple  
677 emission inventories, including EDGAR and MEIC. Although observed atmospheric NH<sub>3</sub>  
678 concentrations have increased over the period 2013–2023, all inventories consistently indicate  
679 a slight decline in NH<sub>3</sub> emissions. This apparent contradiction suggests that the observed rise  
680 in NH<sub>3</sub> concentrations may be primarily driven by reduced emissions of acidifying species—  
681 namely SO<sub>2</sub> and NO<sub>x</sub>—which typically enhance NH<sub>3</sub> partitioning into the particulate phase.  
682 The reductions in SO<sub>2</sub> and NO<sub>x</sub> emissions may have suppressed their atmospheric reactions  
683 with NH<sub>3</sub>, thereby decreasing the formation of particulate ammonium and leaving a greater  
684 fraction of NH<sub>3</sub> un-neutralized in the gas phase. This shift likely contributed to elevated ambient  
685 NH<sub>3</sub> concentrations, as reported in previous studies (Xu et al., 2019a; Liu et al., 2018; Liu et  
686 al., 2017a).

687

688 According to EDGAR data, national SO<sub>2</sub> and NO<sub>x</sub> emissions declined by approximately 20%  
689 from 2013 to 2022, following the implementation of the Air Pollution Prevention and Control  
690 Action Plan in 2013, which led to substantial reductions in these precursor gases. It is important  
691 to note that our Random Forest model does not account for atmospheric chemical processes  
692 involving the formation and partitioning of secondary inorganic aerosols, such as nitrate (NO<sub>3</sub><sup>-</sup>),  
693 sulfate (SO<sub>4</sub><sup>2-</sup>), and ammonium (NH<sub>4</sub><sup>+</sup>). Therefore, for future investigations aiming to quantify  
694 the role of atmospheric chemistry in modulating NH<sub>3</sub> concentrations and deposition, the use of  
695 comprehensive atmospheric chemical transport models such as WRF-Chem or GEOS-Chem is  
696 strongly recommended. These models are capable of resolving multiphase reactions and the  
697 thermodynamic partitioning of NH<sub>3</sub> into the aerosol phase, thereby offering a more mechanistic  
698 understanding of NH<sub>3</sub> dynamics in response to co-emitted precursor changes.

699

700 To further elucidate the drivers of NH<sub>3</sub> dry deposition trends, we employed a logarithmic  
701 differential method to decompose the relative contributions of changes in NH<sub>3</sub> concentrations  
702 and deposition velocities across different land cover types (Figure 10; Table S4, *SI*). All  
703 variables were normalized to facilitate comparison of relative contributions. Results indicate  
704 that variations in NH<sub>3</sub> dry deposition fluxes were predominantly driven by changes in  
705 atmospheric NH<sub>3</sub> concentrations, accounting for approximately 70–80% of the total variation





706 across all land types. Urban areas exhibited the lowest contribution from concentration changes  
707 (72.6%) and the highest from deposition velocity changes (27.4%), likely reflecting the more  
708 complex aerodynamic and surface resistance conditions in urban environments. In contrast,  
709 forested areas showed the highest concentration-driven contribution (81.2%), consistent with  
710 their relatively stable surface characteristics and low anthropogenic disturbance.

711

712 In summary, the observed increase in atmospheric  $\text{NH}_3$  concentrations across China is largely  
713 attributable to the substantial reductions in  $\text{SO}_2$  and  $\text{NO}_x$  emissions. Concurrently, changes in  
714  $\text{NH}_3$  dry deposition fluxes are primarily driven by rising  $\text{NH}_3$  concentrations, which are  
715 indirectly influenced by declining  $\text{SO}_2$  and  $\text{NO}_x$  levels. This inference is supported by  
716 consistent evidence from both satellite and ground-based monitoring networks, which  
717 document a marked decrease in  $\text{SO}_2$  concentrations (Liu M. et al., 2019; Xi et al., 2021)  
718 alongside improvements in acid rain conditions.

719

720 China has made significant progress in controlling acidifying pollutants over the past decades.  
721  $\text{SO}_2$ , a key precursor to acid rain formation, has been regulated since the 1980s, with acid rain  
722 management formally institutionalized in 1990. Between 1993 and 2021, the area affected by  
723 acid rain initially expanded before contracting, reaching a peak in 2015. Since 2006, the acidity  
724 of acid rain has steadily declined (Zhang et al., 2023; Zhao et al., 2010). Although China  
725 initiated acid rain control efforts approximately a decade later than Western countries, it has  
726 achieved more rapid mitigation through the implementation of stringent regulations and  
727 widespread adoption of advanced technologies.

728

729 Previous studies have indicated that optimizing fertilizer application and adjusting protein  
730 content in animal feed could potentially reduce  $\text{NH}_3$  emissions by up to 30% without  
731 compromising agricultural yields or incurring additional costs (Zhang et al., 2020). In contrast,  
732 regulation of  $\text{NH}_3$  emissions has lagged behind that of other pollutants. It was not until the  
733 implementation of the 2018 “Three-Year Action Plan for Winning the Blue-Sky Defense Battle”  
734 that agricultural  $\text{NH}_3$  emissions were formally addressed. This plan emphasized enhanced  
735 recycling of livestock waste and measures to reduce  $\text{NH}_3$  volatilization. Subsequently, the “14th



Five-Year Plan for Energy Conservation and Emission Reduction” further targeted improvements in fertilizer and pesticide use efficiency, setting a goal to reduce  $\text{NH}_3$  emissions from large-scale livestock operations in the Beijing-Tianjin-Hebei region by 5%. Although these recent policies have initiated efforts to mitigate  $\text{NH}_3$  emissions, the rate of reduction remains substantially lower than that achieved for  $\text{SO}_2$ .

The IPCC Sixth Assessment Report (2023) indicates that global surface temperatures increased by approximately  $1.1^\circ\text{C}$  from 2011 to 2020 relative to pre-industrial levels (1850–1900). Continued greenhouse gas emissions are projected to drive further warming. Most Shared Socioeconomic Pathways (SSPs) scenarios forecast global temperature rise reaching  $1.5^\circ\text{C}$  by around 2040, with only the most stringent SSP1-1.9 scenario likely to limit warming below this threshold, necessitating global carbon neutrality by approximately 2055. In the context of future warming, we analyzed projected emissions of  $\text{SO}_2$ ,  $\text{NO}_x$ , and  $\text{NH}_3$  under five SSP scenarios based on the Dynamic Projection Emission Coefficient (DPEC) inventory developed by Tsinghua University (Figure S14, *SI*). All scenarios indicate declining trends for these pollutants; however,  $\text{NH}_3$  exhibits the smallest reduction, amounting to roughly two-thirds of the decreases projected for  $\text{SO}_2$  and  $\text{NO}_x$ . This discrepancy, combined with rising temperatures and decreasing acid gas emissions, is expected to further enhance atmospheric  $\text{NH}_3$  concentrations. Consequently, despite ongoing mitigation efforts targeting  $\text{NH}_3$ , ambient  $\text{NH}_3$  levels may continue to increase. To counteract the synergistic effects of warming and reductions in acid-neutralizing pollutants, more stringent  $\text{NH}_3$  emission control policies will be required in China over the coming decades to effectively stabilize or reduce atmospheric  $\text{NH}_3$  concentrations.

#### 4 Comparison with previous studies and implications

To evaluate and contextualize atmospheric  $\text{NH}_3$  concentrations and dry deposition in China relative to other global regions, we conducted a comprehensive literature review summarized in Table 5. This table integrates the findings of the present study with previous assessments of atmospheric  $\text{NH}_3$  levels and dry deposition fluxes worldwide. The comparative analysis highlights considerable spatial variability, with  $\text{NH}_3$  concentrations ranging from approximately 2 to 10 ppb and area-specific dry deposition fluxes spanning  $0.06$  to  $1.00 \text{ g m}^{-2}$



766  $\text{yr}^{-1}$ . The values reported in this study are generally consistent with those documented in  
767 comparable geographic and climatic regions.

768

769 This study estimates the national average  $\text{NH}_3$  concentration in China at 4.98 ppb and the  
770 corresponding dry deposition flux at  $0.51 \text{ g m}^{-2} \text{ yr}^{-1}$ , and the results for each province of China  
771 were also displayed in Figure S15 (*SI*). The national average results closely align with those of  
772 Liu et al. (2020a), who employed IASI satellite retrievals and reported  $\text{NH}_3$  concentrations of  
773 4.15 ppb and dry deposition fluxes of  $0.58 \text{ g m}^{-2} \text{ yr}^{-1}$ . The Tianjin megacity, Shandong province,  
774 Henan province, Hebei province and Beijing megacity ranked as the largest top 5 regions for  
775  $\text{NH}_3$  concentration and dry deposition flux, where Tianjin and Beijing are located within North  
776 China Plain hotspots, and were largely influenced by atmospheric transport process from nearby  
777 agricultural fields. Compared to Liu et al. (2020a), our analysis extends the observation period  
778 and incorporates calibration against ground-based monitoring data, thereby achieving higher  
779 accuracy. Jia et al. (2016) estimated the global  $\text{NH}_3$  dry deposition flux using empirical models  
780 based on ground station measurements, reporting a value of  $0.68 \text{ g m}^{-2} \text{ yr}^{-1}$  for China.

781

782 In contrast, Xu et al. (2015), utilizing data from the National Nitrogen Deposition Monitoring  
783 Network (NNDMN), reported substantially higher values for China (10.65 ppb and  $1.00 \text{ g m}^{-2}$   
784  $\text{yr}^{-1}$ ), likely reflecting sampling bias due to the predominance of monitoring sites in urban and  
785 agricultural regions characterized by elevated  $\text{NH}_3$  emissions and underrepresentation of  
786 background locations, resulting in overestimation of national averages. Further evidence of  
787 spatial variability is provided by Hu et al. (2020, 2021), who documented significant differences  
788 in  $\text{NH}_3$  concentrations and deposition rates between cropland and forested background sites,  
789 underscoring the critical influence of land use and emission sources on atmospheric  $\text{NH}_3$   
790 dynamics.

791

792 Overall, the synthesis of data summarized in Table 5 indicates that  $\text{NH}_3$  concentrations in China  
793 generally range from 4 to 10 ppb, with corresponding dry deposition fluxes between 0.5 and  
794  $1.0 \text{ g m}^{-2} \text{ yr}^{-1}$ . The observed variability is primarily attributed to differences in observation  
795 periods, measurement methodologies, and spatial coverage. By comparison, the United States



796 exhibits average  $\text{NH}_3$  concentrations of approximately 2.65 ppb and dry deposition fluxes  
797 ranging from 0.07 to 0.3  $\text{g m}^{-2} \text{yr}^{-1}$ , while Europe reports concentrations near 3.13 ppb and  
798 deposition fluxes between 0.1 and 0.3  $\text{g m}^{-2} \text{yr}^{-1}$ . These findings highlight that both  $\text{NH}_3$   
799 concentrations and deposition fluxes in China are substantially higher than those reported for  
800 the United States, Europe, and global averages. Notably, Europe has integrated  $\text{NH}_3$  control  
801 into its air pollution regulatory framework, resulting in measurable emission reductions in  
802 recent years. This experience underscores the importance of implementing more stringent  $\text{NH}_3$   
803 mitigation policies in China to effectively address the ongoing increases in atmospheric  $\text{NH}_3$   
804 concentrations and dry deposition fluxes.

805

806 Previous studies have typically examined either atmospheric  $\text{NH}_3$  concentrations or dry  
807 deposition independently, with relatively few providing a comprehensive assessment  
808 integrating both components. This study addresses this gap by combining satellite-derived  $\text{NH}_3$   
809 concentrations with ground-based observations and utilizing the GEOS-Chem atmospheric  
810 chemistry transport model in conjunction with a machine learning-based Random Forest  
811 algorithm to simulate deposition velocities and fluxes. This integrated approach facilitates the  
812 generation of high-resolution, multi-year estimates of  $\text{NH}_3$  dry deposition across China. The  
813 resulting dataset provides a robust scientific basis for improving national nitrogen management  
814 policies and offers valuable insights into regional and global nitrogen cycling processes.

815

## 816 **5 Conclusions**

817 This study presents a comprehensive analysis of the spatial distribution and temporal trends of  
818 atmospheric ammonia ( $\text{NH}_3$ ) concentrations and dry deposition across China during 2013–2023.

819 The key findings are as follows:

- 820 (1) The North China Plain exhibited persistently high  $\text{NH}_3$  concentrations ( $>10$  ppb), with  
821 significant annual increases in central and eastern regions ( $>0.4$  ppb  $\text{yr}^{-1}$ ). The largest seasonal  
822 increases occurred in summer (0.065 ppb  $\text{yr}^{-1}$ ).  $\text{NH}_3$  concentrations in 2023 were 14%–31%  
823 higher than in 2013 across all seasons. CrIS satellite retrievals were strongly correlated with in-  
824 situ measurements ( $R = 0.79$ ), but are larger than later by a factor of about two.
- 825 (2) The spatial pattern of  $\text{NH}_3$  dry deposition revealed a pronounced east-west gradient, with



826 the highest flux in the North China Plain and Sichuan Basin, and a significant upward trend  
827 along the eastern coast ( $>0.1 \text{ g m}^{-2} \text{ yr}^{-1}$ ). Over the 11-year period,  $\text{NH}_3$  concentrations,  
828 deposition flux, and total deposition increased significantly in the land use types of urban,  
829 cropland, and forest ecosystems. Urban areas showed the highest concentration and deposition  
830 flux as well as the fastest growth rates, while grasslands exhibited the largest total deposition.  
831 (3) The national mean  $\text{NH}_3$  concentration and dry deposition flux were estimated to be 4.98 ppb  
832 and  $0.51 \text{ g m}^{-2} \text{ yr}^{-1}$ , respectively. In addition, our analysis indicated that anthropogenic  
833 emissions were the dominant driver, accounting for approximately 77% of the variance in  $\text{NH}_3$   
834 concentrations, while meteorological conditions explained the remaining 23%; 70%–80% of  
835 deposition changes were governed by atmospheric dynamics. These findings underscore the  
836 increasing  $\text{NH}_3$  pollution across China and provide a critical scientific basis for informed  
837 nitrogen management within one of global largest  $\text{NH}_3$  emission hotspots regions.

838

839 **Data Availability:** CrIS satellite retrievals of  $\text{NH}_3$  were obtained from Environment and  
840 Climate Change Canada (ECCC) at  
841 [https://hpfx.collab.science.gc.ca/~mas001/satellite\\_ext/cris/](https://hpfx.collab.science.gc.ca/~mas001/satellite_ext/cris/) (Shephard et al., 2015; 2020).  
842 Ground-based  $\text{NH}_3$  measurements were sourced from Xu et al. (2019b), available at  
843 <https://www.nature.com/articles/s41597-019-0061-2>.  $\text{NH}_3$  emission inventories were obtained  
844 from the Multi-resolution Emission Inventory for China (MEIC;  
845 [http://meicmodel.org.cn/?page\\_id=560](http://meicmodel.org.cn/?page_id=560)), the Emissions Database for Global Atmospheric  
846 Research (EDGAR v8.1; [https://edgar.jrc.ec.europa.eu/dataset\\_ap81#p3](https://edgar.jrc.ec.europa.eu/dataset_ap81#p3)), and the Dynamic  
847 Projection model for Emissions in China (DPEC; [http://meicmodel.org.cn/?page\\_id=1917](http://meicmodel.org.cn/?page_id=1917)).  
848 Emission data for  $\text{SO}_2$  and  $\text{NO}_x$  were derived from the Inversed Emission Inventory for Chinese  
849 Air Quality (CAQIEI;  
850 <https://www.scidb.cn/en/detail?dataSetId=81cc0de9c68b4a4981e2f295ac612fbf>), the Air  
851 Benefit and Cost and Attainment Assessment System (ABaCAS; [https://abacas-](https://abacas-dss.com/abacasChinese/Default.aspx)  
852 [dss.com/abacasChinese/Default.aspx](https://abacas-dss.com/abacasChinese/Default.aspx)), and the Community Emissions Data System (CEDS;  
853 <https://github.com/JGCRI/CEDS/>). The MEIC and EDGAR inventories were used for both  $\text{NH}_3$   
854 and  $\text{SO}_2/\text{NO}_x$  emissions. Meteorological data were obtained from the ERA5 reanalysis dataset  
855 provided by the European Centre for Medium-Range Weather Forecasts (ECMWF) at



856 <https://cds.climate.copernicus.eu/datasets/reanalysis-era5-single-levels>. Agricultural fertilizer  
857 application data were sourced from the National Bureau of Statistics of China  
858 (<https://www.stats.gov.cn/sj/ndsj/2024/indexch.htm>). Agricultural zoning data were obtained  
859 from the Resource and Environmental Science Data Center  
860 (<https://www.resdc.cn/Default.aspx>), and land cover data were retrieved from the National  
861 Cryosphere Desert Data Center ([https://www.ncdc.ac.cn/portal/metadata/9de270f3-b5ad-4e19-  
862 afc0-2531f3977f2f](https://www.ncdc.ac.cn/portal/metadata/9de270f3-b5ad-4e19-afc0-2531f3977f2f)).

863 **Supplement.** The supplement related to this article is available online

#### 864 **Declaration of Competing Interest**

865 The authors declare that they have no known competing financial interests or personal  
866 relationships that could have appeared to influence the work reported in this paper.

867 **Author contributions:** FS conducted the data analysis and wrote the draft under supervision  
868 of CH, CH designed the study and revised this paper, JS and XL conducted GEOS-Chem  
869 modeling, all other co-authors collected supporting data, read and approved the final manuscript.

#### 870 **Acknowledgments**

871 Cheng Hu is supported by the National Science founding of China (grant nos. 42475125,  
872 42105117, 42021004 and 41975143), this work was also supported by the National Key R&D  
873 Program of China (nos. 2019YFA0607202 and 2020YFA0607501); Jiangsu Science  
874 Foundation for Distinguished Young Scholar (No. BK20220055); The 333 Project of Jiangsu  
875 Province (No. BRA2017402); R&D Foundation of Jiangsu Province, China (No. BK20220020).  
876 Cheng Hu also thanks the founding support from Key Laboratory of Ecosystem Carbon Source  
877 and Sink, China Meteorological Administration (ECSS-CMA202403). We also Sincerely thank  
878 the support from Environment and Climate Change Canada (ECCC) CrIS group.

879

#### 880 **References:**

- 881 Ai X, Hu C, Yang Y, et al. Quantification of Central and Eastern China's atmospheric CH<sub>4</sub> enhancement  
882 changes and its contributions based on machine learning approach. *Journal of Environmental Sciences*,  
883 2024, 138: 236-248.
- 884 Asadi M, McPhedran K N. Greenhouse gas emission estimation from municipal wastewater using a hybrid  
885 approach of generative adversarial network and data-driven modelling. *Science of The Total*



- 886 Environment, 2021, 800: 149508.
- 887 Behera S N, Sharma M, Aneja V P, et al. Ammonia in the atmosphere: a review on emission sources,  
888 atmospheric chemistry and deposition on terrestrial bodies. Environmental Science and Pollution  
889 Research, 2013, 20: 8092-8131.
- 890 Beusen A H W, Bouwman A F, Heuberger P S C, et al. Bottom-up uncertainty estimates of global ammonia  
891 emissions from global agricultural production systems. Atmospheric environment, 2008, 42(24): 6067-  
892 6077.
- 893 Chen J, Cheng M, Krol M, et al. Trends in anthropogenic ammonia emissions in China since 1980: A review  
894 of approaches and estimations. Frontiers in Environmental Science, 2023, 11: 1133753.
- 895 Chen P L, Xiao X X, Wang Q G. High-resolution characteristics of NH<sub>3</sub> emission from 2010 to 2020 in China  
896 based on satellite observation. Environmental Science, 2023, 43(6): 2673-2682.
- 897 Chen Y, Shen H, Kaiser J, et al. High-resolution hybrid inversion of IASI ammonia columns to constrain US  
898 ammonia emissions using the CMAQ adjoint model. Atmospheric chemistry and physics, 2021, 21(3):  
899 2067-2082.
- 900 Dong J, Li B, Li Y, et al. Atmospheric ammonia in China: Long-term spatiotemporal variation, urban-rural  
901 gradient, and influencing factors. Science of The Total Environment, 2023, 883: 163733.
- 902 Eastham S D, Weisenstein D K, Barrett S R H. Development and evaluation of the unified tropospheric–  
903 stratospheric chemistry extension (UCX) for the global chemistry-transport model GEOS-Chem.  
904 Atmospheric Environment, 2014, 89: 52-63.
- 905 Erisman J W, Sutton M A, Galloway J, et al. How a century of ammonia synthesis changed the world. Nature  
906 geoscience, 2008, 1(10): 636-639.
- 907 Flechard C R, Nemitz E, Smith R I, et al. Dry deposition of reactive nitrogen to European ecosystems: a  
908 comparison of inferential models across the NitroEurope network. Atmospheric Chemistry and Physics,  
909 2011, 11(6): 2703-2728.
- 910 Fu X, Wang S, Xing J, et al. Increasing ammonia concentrations reduce the effectiveness of particle pollution  
911 control achieved via SO<sub>2</sub> and NO<sub>x</sub> emissions reduction in east China. Environmental Science &  
912 Technology Letters, 2017, 4(6): 221-227.
- 913 Goldberg D L, Anenberg S C, Lu Z, et al. Urban NO<sub>x</sub> emissions around the world declined faster than  
914 anticipated between 2005 and 2019. Environmental Research Letters, 2021, 16(11): 115004.
- 915 Griffis T J, Hu C, Baker J M, et al. Tall tower ammonia observations and emission estimates in the US



- 916 Midwest. *Journal of Geophysical Research: Biogeosciences*, 2019, 124(11): 3432-3447.
- 917 Hauglustaine D A, Balkanski Y, Schulz M. A global model simulation of present and future nitrate aerosols  
918 and their direct radiative forcing of climate. *Atmospheric Chemistry and Physics*, 2014, 14(20): 11031-  
919 11063.
- 920 He K, Yang F, Ma Y, et al. The characteristics of PM<sub>2.5</sub> in Beijing, China. *Atmospheric Environment*, 2001,  
921 35(29): 4959-4970.
- 922 Hernández D L, Vallano D M, Zavaleta E S, et al. Nitrogen pollution is linked to US listed species declines.  
923 *BioScience*, 2016, 66(3): 213-222.
- 924 Hu C, Griffis T J, Baker J M, et al. Modeling the sources and transport processes during extreme ammonia  
925 episodes in the US Corn Belt. *Journal of Geophysical Research: Atmospheres*, 2020, 125(2):  
926 e2019JD031207.
- 927 Hu C, Griffis T J, Frie A, et al. A multiyear constraint on ammonia emissions and deposition within the US  
928 corn belt. *Geophysical Research Letters*, 2021, 48(6): e2020GL090865.
- 929 IPCC, 2023: *Climate Change 2023: Synthesis Report. Contribution of Working Groups I, II and III to the*  
930 *Sixth Assessment Report of the Intergovernmental Panel on Climate Change* [Core Writing Team, H.  
931 Lee and J. Romero (eds.)]. IPCC, Geneva, Switzerland, pp. 35-115.
- 932 Jia Y, Yu G, Gao Y, et al. Global inorganic nitrogen dry deposition inferred from ground-and space-based  
933 measurements. *Scientific reports*, 2016, 6(1): 19810.
- 934 Kang Y, Liu M, Song Y, et al. High-resolution ammonia emissions inventories in China from 1980 to 2012.  
935 *Atmospheric Chemistry and Physics*, 2016, 16(4): 2043-2058.
- 936 Kharol S K, Shephard M W, McLinden C A, et al. Dry deposition of reactive nitrogen from satellite  
937 observations of ammonia and nitrogen dioxide over North America. *Geophysical Research Letters*, 2018,  
938 45(2): 1157-1166.
- 939 Lei M, Cheng T, Li X, et al. Atmospheric ammonia point source detection technique at regional scale using  
940 high resolution satellite imagery and deep learning. *Atmospheric Research*, 2021, 257: 105587.
- 941 Liu L, Wen Z, Liu S, et al. Decline in atmospheric nitrogen deposition in China between 2010 and 2020.  
942 *Nature Geoscience*, 2024, 17(8): 733-736.
- 943 Liu L, Zhang X, Wong A Y H, et al. Estimating global surface ammonia concentrations inferred from satellite  
944 retrievals. *Atmospheric Chemistry and Physics*, 2019, 19(18): 12051-12066.
- 945 Liu L, Zhang X, Xu W, et al. Global estimates of dry ammonia deposition inferred from space-measurements.





- 946 Science of the Total Environment, 2020a, 730: 139189.
- 947 Liu L, Zhang X, Xu W, et al. Ground ammonia concentrations over China derived from satellite and  
948 atmospheric transport modeling. Remote Sensing, 2017a, 9(5): 467.
- 949 Liu L, Zhang X, Xu W, et al. Reviewing global estimates of surface reactive nitrogen concentration and  
950 deposition using satellite retrievals. Atmospheric Chemistry and Physics, 2020b, 20(14): 8641-8658.
- 951 Liu L, Zhang X, Xu W, et al. Temporal characteristics of atmospheric ammonia and nitrogen dioxide over  
952 China based on emission data, satellite observations and atmospheric transport modeling since 1980.  
953 Atmospheric Chemistry and Physics, 2017b, 17(15): 9365-9378.
- 954 Liu M, Huang X, Song Y, et al. Ammonia emission control in China would mitigate haze pollution and  
955 nitrogen deposition, but worsen acid rain. Proceedings of the National Academy of Sciences, 2019,  
956 116(16): 7760-7765.
- 957 Liu M, Huang X, Song Y, et al. Rapid SO<sub>2</sub> emission reductions significantly increase tropospheric ammonia  
958 concentrations over the North China Plain. Atmospheric Chemistry and Physics, 2018, 18(24): 17933-  
959 17943.
- 960 Liu S, Xu H, Wang J, et al. Evidence for global increases in urban ammonia pollution and their drivers.  
961 Science of the Total Environment, 2024, 955: 176846.
- 962 Lu X, Liu Y, Su J, et al. Tropospheric ozone trends and attributions over East and Southeast Asia in 1995 –  
963 2019: An integrated assessment using statistical methods, machine learning models, and multiple  
964 chemical transport models. EGU sphere, 2024, 2024: 1-65.
- 965 Lu X, Zhang L, Wu T, et al. Development of the global atmospheric chemistry general circulation model  
966 BCC-GEOS-Chem v1. 0: model description and evaluation[J]. Geoscientific model development, 2020,  
967 13(9): 3817-3838.
- 968 Ma S. High-resolution assessment of ammonia emissions in China: Inventories, driving forces and mitigation.  
969 Atmospheric Environment, 2020, 229: 117458.
- 970 Na K, Song C, Switzer C, et al. Effect of ammonia on secondary organic aerosol formation from  $\alpha$ -pinene  
971 ozonolysis in dry and humid conditions. Environmental science & technology, 2007, 41(17): 6096-6102.
- 972 Paulot F, Jacob D J, Pinder R W, et al. Ammonia emissions in the United States, European Union, and China  
973 derived by high-resolution inversion of ammonium wet deposition data: Interpretation with a new  
974 agricultural emissions inventory (MASAGE\_NH<sub>3</sub>). Journal of Geophysical Research: Atmospheres,  
975 2014, 119(7): 4343-4364.



- 976 Phillips S B, Aneja V P, Kang D, et al. Modelling and analysis of the atmospheric nitrogen deposition in  
977 North Carolina. *International journal of global environmental issues*, 2006, 6(2-3): 231-252.
- 978 Pinder R W, Adams P J, Pandis S N. Ammonia emission controls as a cost-effective strategy for reducing  
979 atmospheric particulate matter in the eastern United States. 2007.
- 980 Pinder R W, Gilliland A B, Dennis R L. Environmental impact of atmospheric NH<sub>3</sub> emissions under present  
981 and future conditions in the eastern United States. *Geophysical Research Letters*, 2008, 35(12).
- 982 Russell K M, Keene W C, Maben J R, et al. Phase partitioning and dry deposition of atmospheric nitrogen at  
983 the mid-Atlantic US coast. *Journal of Geophysical Research: Atmospheres*, 2003, 108(D21).
- 984 Shao S C, Chang Y H, Cao F, et al. High-frequency evolution of urban atmospheric ammonia and ammonium  
985 and its gas-to-particle conversion mechanism in Nanjing City. *Huan Jing ke Xue= Huanjing Kexue*,  
986 2019, 40(10): 4355-4363.
- 987 Shephard M W, Cady-Pereira K E. Cross-track Infrared Sounder (CrIS) satellite observations of tropospheric  
988 ammonia. *Atmospheric Measurement Techniques*, 2015, 8(3): 1323-1336.
- 989 Shephard M W, Damers E, Cady-Pereira K E, et al. Ammonia measurements from space with the Cross-  
990 track Infrared Sounder: characteristics and applications. *Atmospheric Chemistry and Physics*, 2020,  
991 20(4): 2277-2302.
- 992 Someya Y, Imasu R, Shiomi K, et al. Atmospheric ammonia retrieval from the TANSO-FTS/GOSAT thermal  
993 infrared sounder. *Atmospheric Measurement Techniques*, 2020, 13(1): 309-321.
- 994 Song X. Study on the present situation and countermeasures of agricultural sustainable development  
995 in Huang-Huai-Hai Plain. *Agricultural Science*, 2024, 7(5): 74-76.
- 996 Van Damme M, Clarisse L, Franco B, et al. Global, regional and national trends of atmospheric ammonia  
997 derived from a decadal (2008–2018) satellite record. *Environmental Research Letters*, 2021, 16(5):  
998 055017.
- 999 Van Damme M, Clarisse L, Whitburn S, et al. Industrial and agricultural ammonia point sources exposed.  
1000 *Nature*, 2018, 564(7734): 99-103.
- 1001 Van Der Graaf S, Damers E, Schaap M, et al. How are NH<sub>3</sub> dry deposition estimates affected by combining  
1002 the LOTOS-EUROS model with IASI-NH<sub>3</sub> satellite observations?. *Atmospheric Chemistry and Physics*,  
1003 2018, 18(17): 13173-13196.
- 1004 Van Der Graaf S, Damers E, Segers A, et al. Data assimilation of CrIS NH<sub>3</sub> satellite observations for  
1005 improving spatiotemporal NH<sub>3</sub> distributions in LOTOS-EUROS. *Atmospheric Chemistry and Physics*,



- 1006 2022, 22(2): 951-972.
- 1007 Wang R, Pan D, Guo X, et al. Bridging the spatial gaps of the Ammonia Monitoring Network using satellite  
1008 ammonia measurements. *Atmospheric Chemistry and Physics*, 2023, 23(20): 13217-13234.
- 1009 Warner J X, Dickerson R R, Wei Z, et al. Increased atmospheric ammonia over the world's major agricultural  
1010 areas detected from space. *Geophysical Research Letters*, 2017, 44(6): 2875-2884.
- 1011 White E, Shephard M W, Cady-Pereira K E, et al. Accounting for non-detects: Application to satellite  
1012 ammonia observations. *Remote sensing*, 2023, 15(10): 2610.
- 1013 Wu Y, Gu B, Erisman J W, et al. PM<sub>2.5</sub> pollution is substantially affected by ammonia emissions in China.  
1014 *Environmental pollution*, 2016, 218: 86-94.
- 1015 Xi Y, Zhu J, Zhang Q, et al. Hysteresis response of wet nitrate deposition to emission reduction in Chinese  
1016 terrestrial ecosystems. *Atmospheric Environment*, 2021, 260: 118555.
- 1017 Xu W, Liu X, Liu L, et al. Impact of emission controls on air quality in Beijing during APEC 2014:  
1018 Implications from water-soluble ions and carbonaceous aerosol in PM<sub>2.5</sub> and their precursors.  
1019 *Atmospheric Environment*, 2019a, 210: 241-252.
- 1020 Xu W, Luo X S, Pan Y P, et al. Quantifying atmospheric nitrogen deposition through a nationwide monitoring  
1021 network across China. *Atmospheric Chemistry and Physics*, 2015, 15(21): 12345-12360.
- 1022 Xu W, Zhang L, Liu X. A database of atmospheric nitrogen concentration and deposition from the nationwide  
1023 monitoring network in China. *Scientific data*, 2019b, 6(1): 51.
- 1024 Yang J, Huang X. The 30\,m annual land cover dataset and its dynamics in China from 1990 to 2019. *Earth  
1025 System Science Data*, 2021, 13, (8): 3907-3925.
- 1026 Zavalov V, Esplin M, Scott D, et al. Noise performance of the CrIS instrument. *Journal of Geophysical  
1027 Research: Atmospheres*, 2013, 118(23): 13,108-13,120.
- 1028 Zeng, Z.-C., Lee, L., Qi, C., L. Clarisse, and M. Van Damme, Optimal estimation retrieval of tropospheric  
1029 ammonia from the Geostationary Interferometric Infrared Sounder onboard FengYun-4B, *Atmospheric  
1030 Measurement Techniques*, 2023, 16, 3693–3713, <https://doi.org/10.5194/amt-16-3693-2023>.
- 1031 Zhan X, Adalibieke W, Cui X, et al. Improved estimates of ammonia emissions from global croplands.  
1032 *Environmental Science & Technology*, 2020, 55(2): 1329-1338.
- 1033 Zhang D, Xu R, Zhao Y, et al. Interannual variation characteristics of acid rain from 2006-2021 in China.  
1034 *Environmental Pollution and Control*, 2023, 45(06): 849-854.
- 1035 Zhang J, Ji D, Hu C, et al. Multiple-model based simulation of urban atmospheric methane concentration and



- 1036 the attributions to its seasonal variations: A case study in Hangzhou megacity, China. *Environmental*  
1037 *Pollution*, 2024, 361: 124781.
- 1038 Zhang L, Jacob D J, Knipping E M, et al. Nitrogen deposition to the United States: distribution, sources, and  
1039 processes. *Atmospheric Chemistry and Physics*, 2012, 12(10): 4539-4554.
- 1040 Zhang X, Gu B, van Grinsven H, et al. Societal benefits of halving agricultural ammonia emissions in China  
1041 far exceed the abatement costs. *Nature communications*, 2020, 11(1): 4357.
- 1042 Zhao Y, Hou Q. Characteristics of the Acid Rain Variation in China During 1993-2006 and Associated Causes.  
1043 *Acta Meteorologica Sinica*, 2010, 24(02): 239-250.
- 1044 Zhu L, Henze D K, Bash J O, et al. Sources and impacts of atmospheric NH<sub>3</sub>: current understanding and  
1045 frontiers for modeling, measurements, and remote sensing in North America. *Current Pollution Reports*,  
1046 2015, 1: 95-116.
- 1047

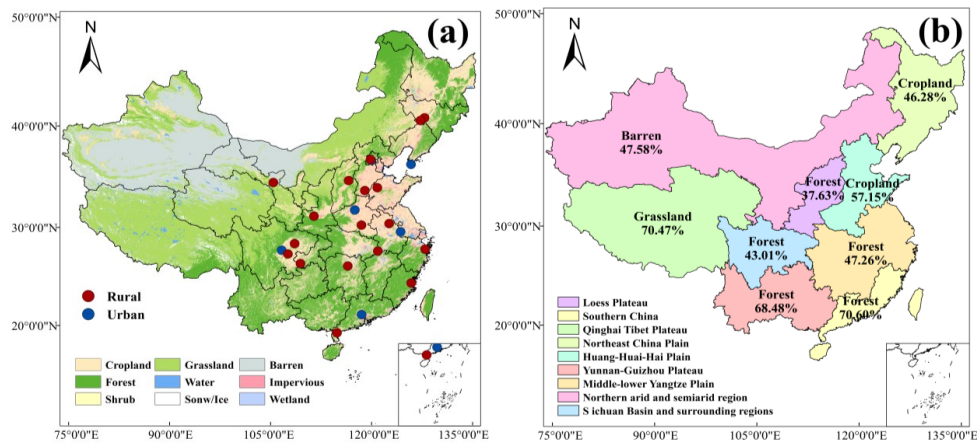


**Figure 1.** (a) Spatial distribution of land use types and NH<sub>3</sub> monitoring sites in China in 2022, (b) classification of China into nine major agroecological zones based on agricultural practices and climatic conditions.

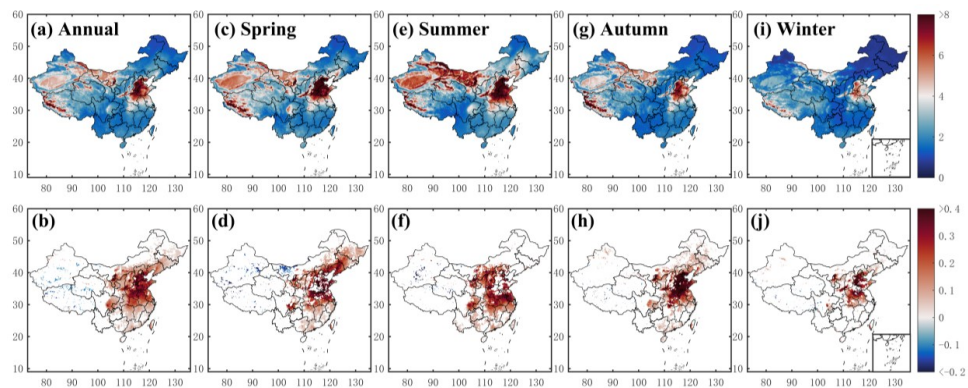


**Figure 2.** Spatial distribution and temporal trends of annual and seasonal  $\text{NH}_3$  concentrations in China from 2013 to 2023 (Units: ppb for concentration;  $\text{ppb yr}^{-1}$  for trend).

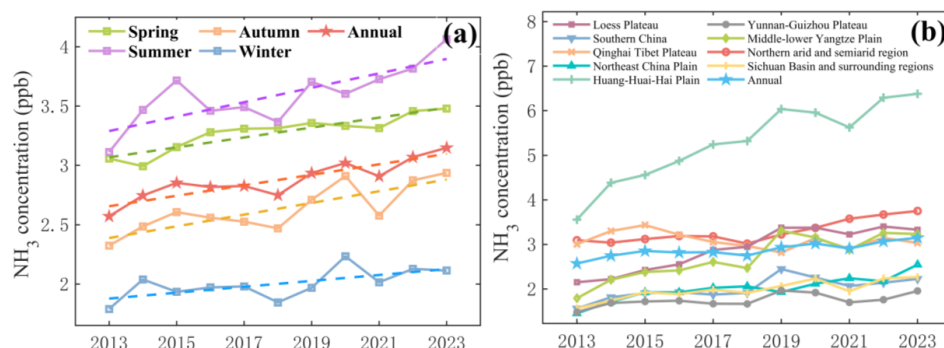


**Figure 3.** (a) Seasonal and (b) regional variations in  $\text{NH}_3$  concentrations across China from 2013 to 2023 (Unit: ppb).

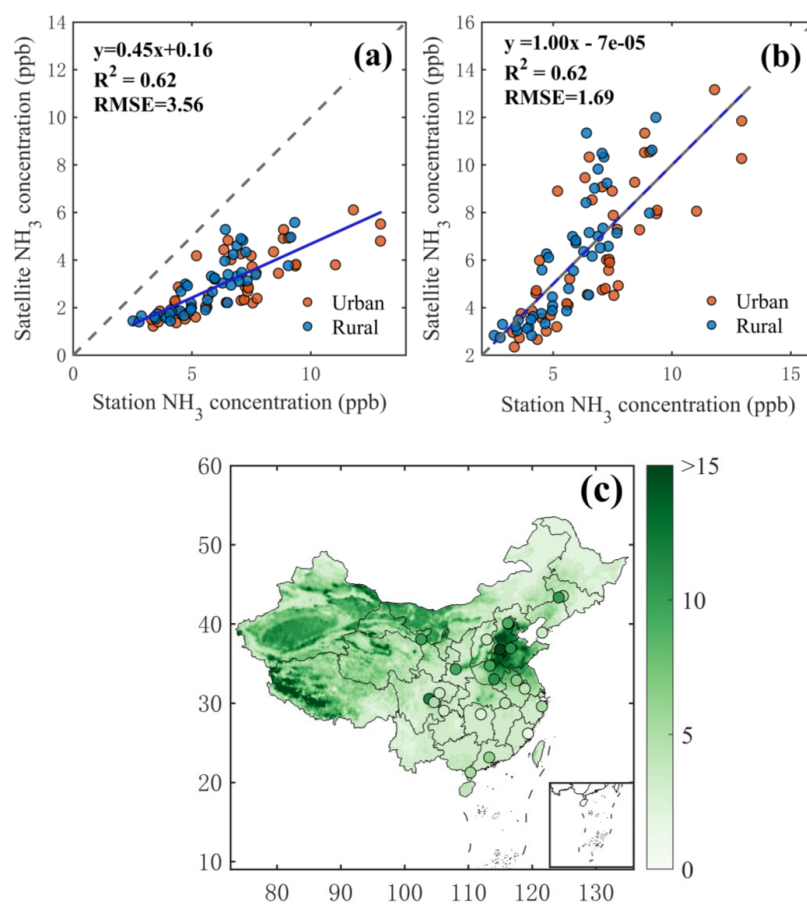


**Figure 4.** Comparison between satellite and ground-based  $\text{NH}_3$  observations: (a) correlation between satellite-derived and ground-based  $\text{NH}_3$  concentrations; (b) correlation after correction of satellite-derived  $\text{NH}_3$  concentrations; (c) comparison of corrected satellite-derived and ground-based  $\text{NH}_3$  concentrations in 2015 (Unit: ppb).



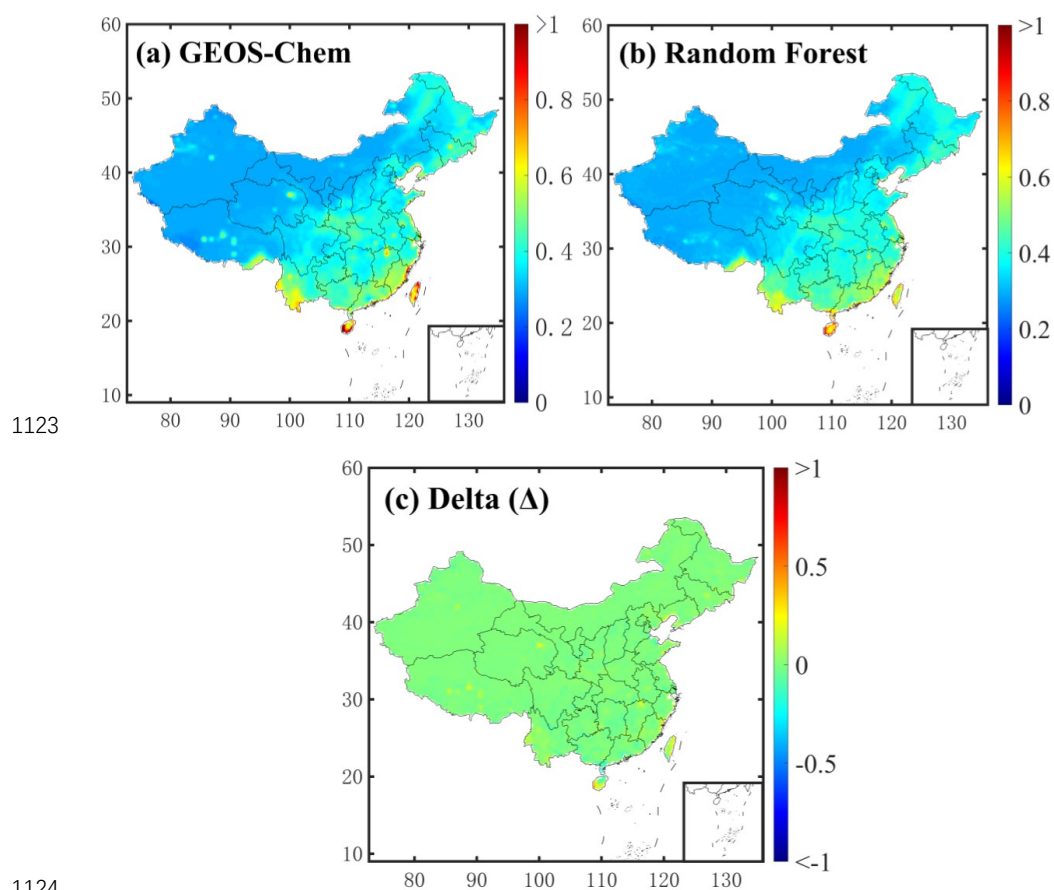


**Figure 5.** NH<sub>3</sub> dry deposition velocity in China in 2015: (a) GEOS-Chem simulation; (b) Random forest simulation; (c) Model difference (Unit: cm·s<sup>-1</sup>)

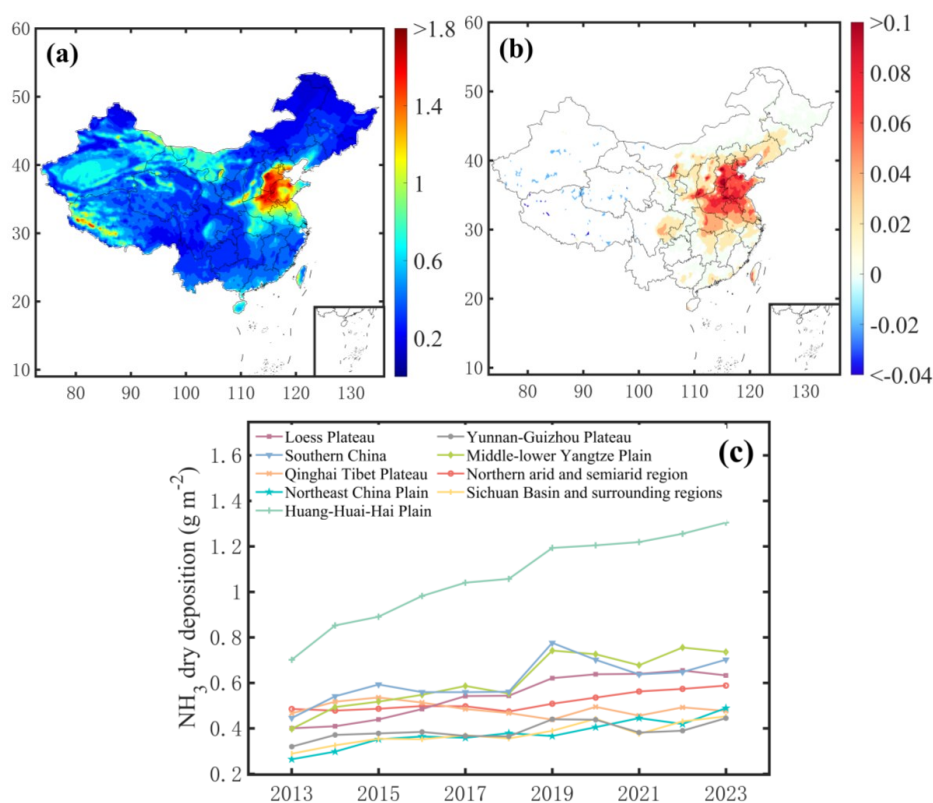


**Figure 6.** Spatial and regional trends in annual mean  $\text{NH}_3$  dry deposition in China from 2013 to 2023: (a) spatial distribution of annual mean  $\text{NH}_3$  dry deposition (Unit:  $\text{g m}^{-2}$ ); (b) temporal trend of  $\text{NH}_3$  dry deposition (Unit:  $\text{g m}^{-2} \cdot \text{yr}^{-1}$ ); (c) interannual variation of  $\text{NH}_3$  dry deposition across different regions (Unit:  $\text{g m}^{-2}$ ).

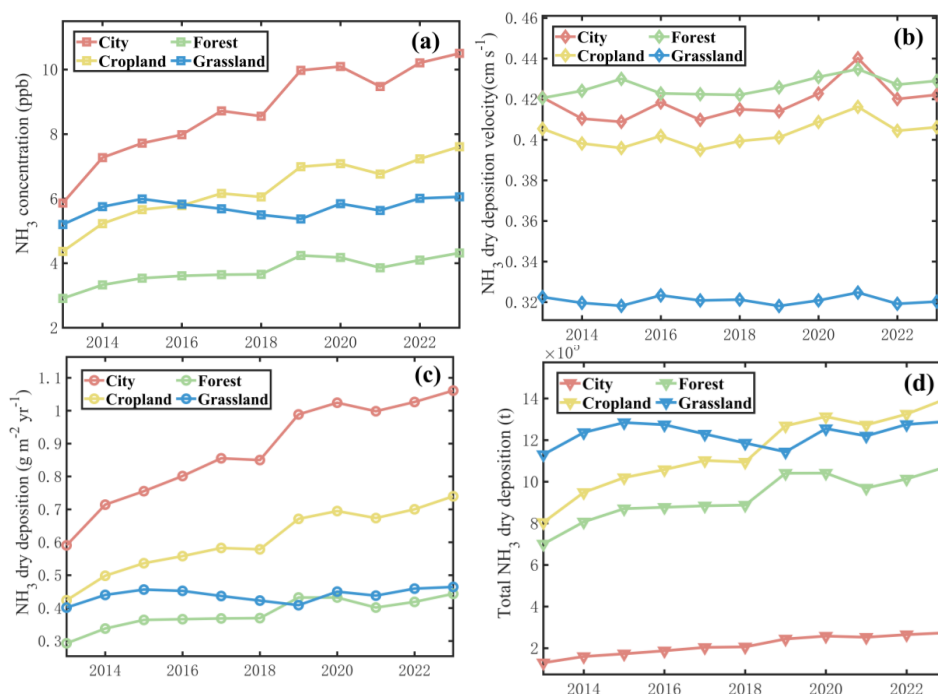


**Figure 7.** Trends in NH<sub>3</sub> concentration, dry deposition velocity, and dry deposition amount in China from 2013 to 2023: (a) trends in corrected NH<sub>3</sub> concentrations across different land surface types (Unit: ppb); (b) NH<sub>3</sub> dry deposition velocities over different land surface types (Unit: cm·s<sup>-1</sup>); (c) trends in NH<sub>3</sub> dry deposition flux per unit area over different land surface types (Unit: g·m<sup>-2</sup>); (d) interannual variation in total NH<sub>3</sub> dry deposition over different land surface types (Unit: t).

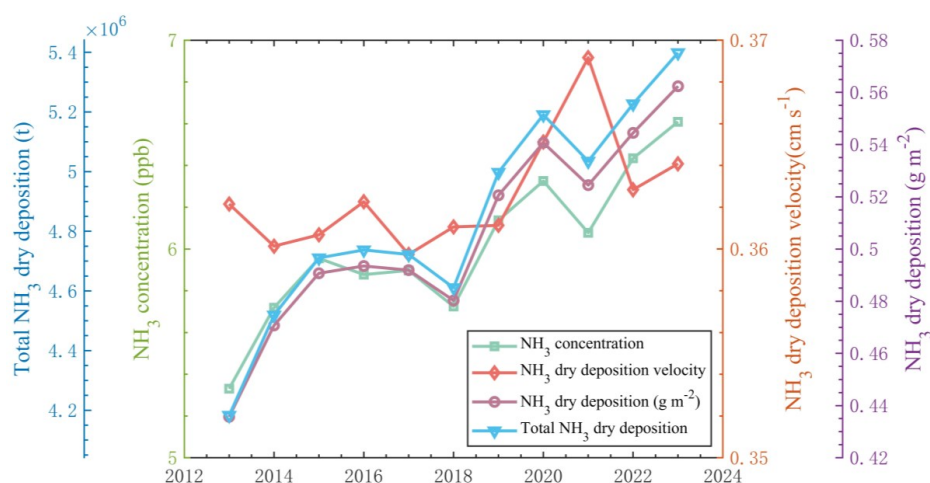


**Figure 8.** Annual changes in NH<sub>3</sub> concentration, dry deposition velocity, dry deposition flux and total dry deposition for China from 2013 to 2023;

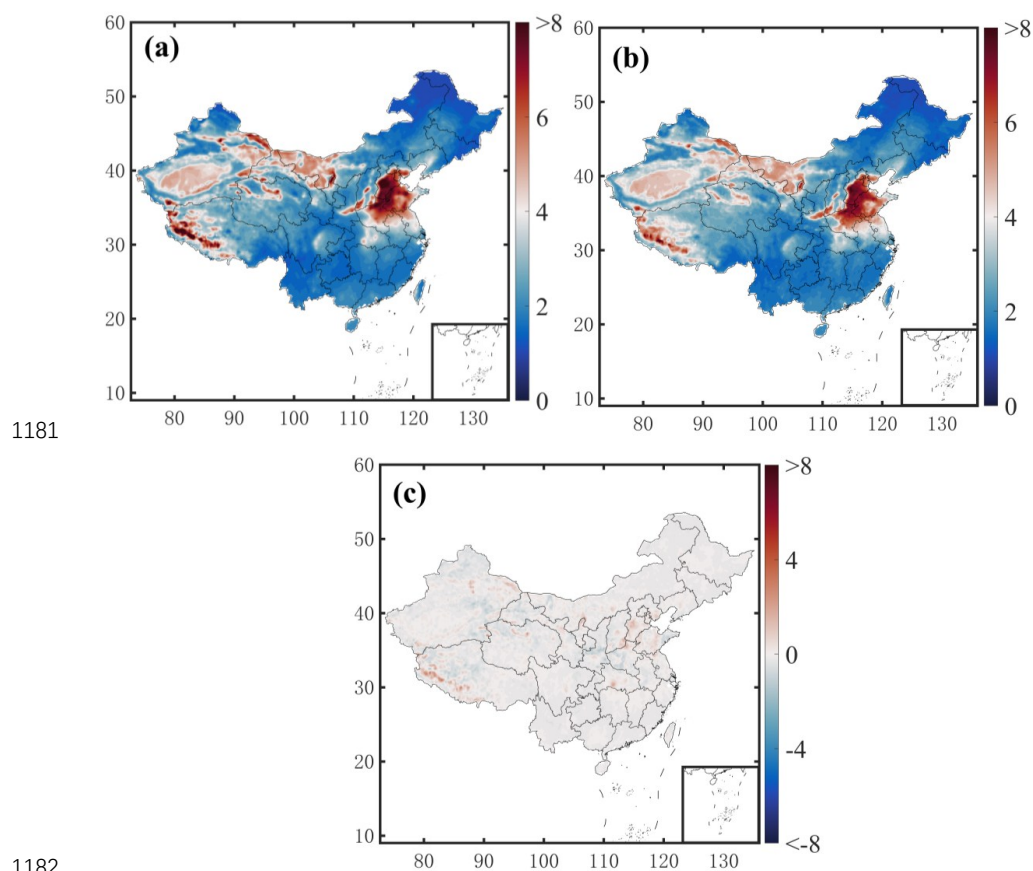


**Figure 9.** (a) Spatial distribution of satellite-based observation of  $\text{NH}_3$  concentration for averages between 2013 and 2023, (b) simulation of  $\text{NH}_3$  concentration by RF model for averages between 2013 and 2023, (c) difference between observation and model simulation, Units: ppb.

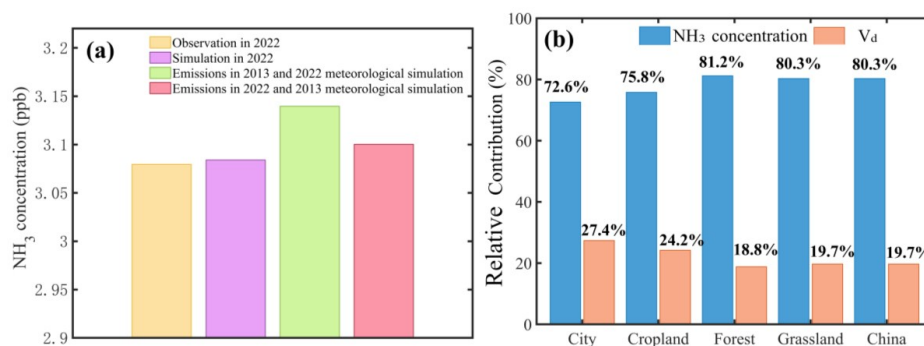


**Figure 10.** (a) The contribution of emissions and meteorological factors to the variation of NH<sub>3</sub> concentration; (b) The relative contribution of NH<sub>3</sub> concentration and dry deposition velocity to the dry deposition flux changes.



1210 **Table 1.** Dominant underlying surface types and their proportional area coverage in each  
1211 defined region.

Agricultural zoning	Main underlying surface type	Area proportion
Northeast China Plain	Cropland	46.28%
Yunnan-Guizhou Plateau	Forest	68.48%
Northern arid and semiarid region	Barren	47.58%
Southern China	Forest	70.60%
Sichuan Basin and surrounding regions	Forest	43.01%
Middle-lower Yangtze Plain	Forest	47.26%
Qinghai Tibet Plateau	Grassland	70.47%
Loess Plateau	Forest	37.63%
Huang-Huai-Hai Plain	Cropland	57.15%

1212  
1213  
1214  
1215  
1216  
1217  
1218  
1219  
1220  
1221  
1222  
1223  
1224  
1225  
1226  
1227  
1228



**Table 2.** Annual and seasonal average NH<sub>3</sub> concentrations and their annual mean increase rates.

Season	NH <sub>3</sub> concentration (ppb)	Annual growth in NH <sub>3</sub> concentration (ppb yr <sup>-1</sup> )
Annual	2.88	0.045
Spring	3.28	0.039
Summer	3.59	0.065
Autumn	2.63	0.050
Winter	2.00	0.023





1251 **Table 3.** Average  $\text{NH}_3$  concentration per unit area and annual mean increment and corrected  
1252  $\text{NH}_3$  concentration in the nine major agricultural regions of China from 2013 to 2023.

Agricultural zoning	$\text{NH}_3$ concentration (ppb)	Annual growth in $\text{NH}_3$ concentration (ppb yr <sup>-1</sup> )	Corrected $\text{NH}_3$ concentration (ppb)
Huang-Huai-Hai Plain	5.29	0.24	11.36
Northern arid and semiarid region	3.29	0.08	6.93
Qinghai Tibet Plateau	3.09	-0.03	6.48
Loess Plateau	2.90	0.14	6.05
Middle-lower Yangtze Plain	2.70	0.13	5.62
Southern China	2.01	0.06	4.09
Northeast China Plain	2.01	0.08	4.09
Sichuan Basin and surrounding regions	1.98	0.06	4.02
Yunnan-Guizhou Plateau	1.75	0.03	3.52

1253



**Table 4.** Average  $\text{NH}_3$  dry deposition per unit area and annual mean increment in the nine major agricultural regions of China from 2013 to 2023.

Agricultural zoning	Dry deposition of $\text{NH}_3$ ( $\text{g m}^{-2}$ )	Annual growth		Dry deposition of $\text{NH}_3$ ( $\text{g m}^{-2}$ )	Annual growth of $\text{NH}_3$ dry deposition ( $\text{g m}^{-2} \text{ yr}^{-1}$ )
		of $\text{NH}_3$ dry deposition ( $\text{g m}^{-2} \text{ yr}^{-1}$ )	Agricultural zoning		
Huang-Huai-Hai Plain	1.064	0.054	Southern China	0.486	0.020
Northern arid and semiarid region	0.612	0.012	Northeast	0.389	0.018
			China Plain		
			Sichuan Basin		
Qinghai Tibet Plateau	0.611	-0.004	and surrounding regions	0.377	0.014
			Yunnan-		
			Guizhou Plateau		
Loess Plateau	0.546	0.030		0.376	0.008
Middle-lower Yangtze Plain	0.517	0.034			



**Table 5.** Comparison of global and regional NH<sub>3</sub> concentrations and dry deposition rates across different studies. note: All results have been standardized to uniform units.

Reference	Study period	Study region	NH <sub>3</sub> dry deposition (g m <sup>-2</sup> yr <sup>-1</sup> )		NH <sub>3</sub> concentration (ppb)	
This study	2013-2023	China	City	0.88	City	8.76
			Forest	0.38	Forest	3.76
			Cropland	0.61	Cropland	6.27
			Grassland	0.44	Grassland	5.72
			China	0.51	China	4.98
		Global	0.17		--	
					Crop	8.04
					Urban	6.86
					Forest	4.66
		China	0.58		Grass	3.10
					Grass	3.37
					Mean	4.15
					Crop	4.00
					Urban	4.52
Liu et al., 2020a	2008-2016	Europe	0.36		Forest	3.32
					Grass	2.34
					Grass	1.87
					Mean	3.13
					Crop	4.38
		US	0.26		Urban	3.10
					Forest	2.51
					Grass	2.91
					Grass	1.87
					Mean	2.65
Jia et al., 2016	2005–2014	Asia (China)	0.29 (0.68)		--	
		North America	0.042 (0.078)		--	



		(US)				
		Europe	0.11	--		
		Africa	0.32	--		
		South America	0.12	--		
		Oceania	0.037	--		
		Global land	0.18	--		
	2013 warm season	North America	0.06-1.22	--		
Kharol et al., 2018	(April–	USA	0.27	--		
	September)	Canada	0.18	--		
Zhang et al. 2012	2006–2008	US	0.11	--		
		China	--		4.15 (0.39-22.90)	
Liu et al., 2019	2008-2016	Europe	--		3.14 (0.07-16.58)	
		US	--		2.66 (0.24-18.52 )	
Xu et al., 2015	2010-2014	China	1.00 (0.06-1.95)		10.65 (0.52-22.89)	
Phillips et al., 2006	1999 Summer	North Carolina	0.36	--		
		Tall-tower (100 m) observations	Forested lands	0.10-0.16	56 m	6.76
Hu et al., 2020	November 2017	in Minnesota	Agricultural lands	0.41-0.62	100 m	6.64
Shao et al., 2019	October - November 2018	Nanjing	--		21.96±9.61	
			Forested lands	0.054±0.0054,	Forested lands	0.58±0.12,
				0.059±0.011,		0.71±0.14,
				0.059±0.011		0.60±0.12
Hu et al., 2021	2017-2019 warm season	US Corn Belt		0.77±0.16,		6.87±1.4,
			Agricultural lands	0.76±0.16,	Agricultural lands	6.76±1.4,
				0.77±0.16		6.48±1.3




---

			LOTOS-		
Van Der Graaf	2014 warm season	Europe	EUROS	0.21	--
et al., 2018			model		
			IASI	0.27	

---

1269

1270

1271

1272

1273

1274

1275